Geomech. Geophys. Geo-energ. Geo-resour. (2026) 12:65
https://doi.org/10.1007/s40948-025-01087-2

RESEARCH

Influence of mineralogical heterogeneities on the mechanical behavior of a shear zone in gneiss, Schauinsland Mine, Germany

Lena Muhl · Benjamin Avakian · Guido Blöcher · Ingo Sass · Ghislain Trullenque

Received: 2 June 2025 / Accepted: 6 December 2025

Abstract Enhanced geothermal systems including fault zones and fracture systems are characterized by geological heterogeneities leading to area dependent mechanical behavior. The interplay between fault zone porosity architecture and mechanical behavior is a key factor to understand the fault zone tectonic stability. Through the sampling across a clay-rich shear zone including host rock, transition zone and next to the main core zone, mechanical and mineralogical investigations presented a transition from a brittle to ductile failure behavior towards the main core zone. High compressive strength values were achieved for rock samples with high clay content which is an indicator of the reorganization of strong mineral phases within a weak compacted clayey matrix. Moreover, tensile strength parameters portrayed a decrease in strength towards the main core zone presenting a weakening effect due to the mineralogical composition. The increase in clay content related to the hydrothermal alteration of primary biotite and feldspar into clay minerals led to an increase in porosity. These different strength and hydraulic behaviors demonstrate the importance of the combined analysis of different disciplines to identify fault zone areas which are sustainable for geothermal exploitation.

Supplementary Information The online version contains supplementary material available at https://doi.org/10.1007/s40948-025-01087-2.

L. Muhl (✉) · G. Blöcher · I. Sass
GFZ Helmholtz Centre for Geosciences, Section 4.3: Geoenergy, Telegrafenberg, 14473 Potsdam, Germany
e-mail: Lena.muhl@gfz.de

L. Muhl · I. Sass
Department of Geothermal Science and Technology, Institute of Applied Geosciences, Technical University of Darmstadt, Schnittspahnstraße 9, 64287 Darmstadt, Germany

B. Avakian
CY Cergy Paris Université, Sorbonne Université, CNRS, Institut des Sciences de la Terre de Paris, ISTeP, 1 Rue Descartes, 95000 Neuville-sur-Oise, France

B. Avakian
Archaeology, Environmental Changes & Geo-Chemistry, Vrije Universiteit Brussel, Pleinlaan 2, 1050 Brussels, Belgium

B. Avakian · G. Trullenque
UniLaSalle, B2R (U2R 7511) UPJV-UNIL, 19 Rue Pierre Waguet, 60000 Beauvais, France

G. Blöcher
TU Berlin, Department of Engineering Geology, 10587 Berlin, Germany

Published online: 27 March 2026

Article Highlights

- Mineralogical anisotropy and hydrothermal alteration strongly influence the mechanical behavior of fault zone rocks
- Host rock and main core samples show high strength, though one behaves brittle and the other ductile
- Transition zone of the fault is the weakest, showing both elastic and plastic characteristics with low strength

Keywords Geothermal · fault zones · Mechanical parameters · Clay gouge · Weakening effect

1 Introduction

Crystalline rocks are naturally low in porosity and permeability. Brittle fault zones, in which permeability is higher than that of the matrix, likely provide fluid pathways within the rock mass (Caine et al. 1996; Faulkner et al. 2008; Fossen and Cavalcante 2017). Associated fault networks constitute key targets for geothermal exploitation (Lee et al. 2011; Hofmann et al. 2014; Garcia et al. 2016; Ledingham et al. 2019; Bischoff et al. 2024) and are of particular interest for geothermal operations in the Upper Rhine Graben (Genter et al. 1996; Baujard et al. 2017; Glaas et al. 2021). Fault damage and core zones (Caine et al. 1996), along with associated open fractures in the crystalline matrix, act as fluid flow pathways in reservoirs (Avakian et al. 2025). Fault zones can be detected by geophysical exploration, investigated by drilling and characterized by sectional analysis or borehole logging. They are identified via the degree of deformation and hydrothermal alteration, which serve as a proxy for porosity and permeability (Genter et al. 2010; Meller and Ledésert 2017; Jones et al. 2024).

Fault zone internal properties such as permeability, mechanical strength and mineralogy vary over their seismic cycle (Callahan et al. 2020; Avakian et al. 2025). This variation is coupled with deformation and fluid/rock interaction processes which may alter the fault zone from a conduit to a barrier (Faulkner et al. 2010; Klee et al. 2021b). Throughout the seismic cycle of a single or multi-core fault zone, the highest fluid flow rate occurs immediately after its reactivation, triggering hydrothermal alteration processes. On the one hand, porosity can be increased by dissolving the primary mineral phases or by forming interparticle voids through crushing (Caine et al. 1996; Faulkner et al. 2010; Bischoff et al. 2024). On the other hand, precipitation of secondary phases and rearrangement of fault gouge particles reduce porosity and henceforth the permeability (Ledésert et al. 1999; Callahan et al. 2020). Minerals arising from hydrothermal alteration influence the strength of fault zones (Tenthorey and Cox 2006). Quartz or carbonate precipitation strengthens the fault rock while clay weakens the structure (Lu and He 2018). Moreover, the interseismic phase can lead to grain reorganization and compaction which enhances cohesion of the sample (Sibson 1992). The repetition of these processes through the fault zone seismic cycle leads to highly heterogeneous structures with complex mechanical properties.

Fracture networks, deformation, and hydrothermal alteration within fault zones must be analyzed to characterize their associated fluid pathways and mechanical behavior. Heterogeneities such as foliation or clay gouge layers related to hydrothermal alteration processes within the rock affect its hydraulic and mechanical properties (Lu and He 2018; Acosta and Violay 2020; Bedford et al. 2022). Deformations and discontinuities can be concentrated within mineralogical layering (e.g., gneiss) (Bai and Young 2020). The mechanical heterogeneity between a clay-rich gouge, developed from the alteration of k-feldspar, biotite or plagioclase, and a crystalline rock could favor the response of a fault zone to shear, where sliding rather than opening occurs at frictionally weak discontinuities (Morrow et al. 1984; Logan and Rauenzahn 1987). Fault zone weakening related to clay-rich gouges and hydraulic over pressure might affect the fracture distribution and lead to preferential fluid pathways (Lu and He 2018; Callahan et al. 2020) along with changes in failure mode from brittle to plastic (Marone 1995). These parameters must therefore be taken into account in the treatment of heterogeneous fault zones, and detailed investigations of such structures is required.

Collecting fault zone material from wells is mostly limited to cuttings, which have limited value for precise sampling and analysis. Cuttings can provide some information about the bulk rock type, but they lack

visual details such as open fractures or gouges, making it difficult to understand the internal structure of the fault zone. In order to characterize the fault zones in the geothermal reservoirs of the Upper Rhine Graben (URG), an analogue fault in a mine in the Black Forest is investigated in this study. The analogue is defined as a geological exposure that has undergone similar geological events as an in-depth structure and may provide evidence about formation processes (Dezayes et al. 2021). This approach is already widely accepted for geothermal reservoir characterization (Bertrand et al. 2021; Chabani et al. 2021; Dezayes et al. 2021; Klee et al. 2021a, 2021b; Bossennec et al. 2022; Peacock et al. 2022; Schulz et al. 2022).

In this work, the analogue corresponds to a fossilized shear zone in a gallery of the Schauinsland Mine, dug into a gneissic host rock in the Black Forest (Germany). The analogue provides a 3D view of a clay-rich shear zone with a multi-core architecture. The shear zone was cut perpendicularly by a dextral transtensive shearing structure and later filled with silver-bearing ore (Werner et al. 2002; Avakian et al. 2025). Mechanical investigations were carried out on rocks from the main core zone of the structure, including uniaxial and triaxial as well as tensile strength measurements. These are linked to porosity, permeability, and mineralogical characterizations of the samples, to investigate the opening of the ore vein structure in a mineralogically heterogeneous shear zone. In addition, this study investigates how hydraulic pressure and mechanical weakening influence the opening of fractures in weak fault planes, which is critical for understanding fault zone behavior. For reservoir characterization, it also provides insights into the permeability distribution and the possible reactivation of existing structures.

2 Geological setting

The Upper Rhine Graben (URG), part of the European Cenozoic Rift System (Fig. 1a), is oriented NNE, with a length of 300 km and a width of 30–40 km (Fig. 1b; Ziegler 1992). Bounded by NNE-trending normal faults, the URG is bordered by the Vosges Massif to the west and the Black Forest to the east. The Variscan basement of the URG is mainly covered by Mesozoic and Cenozoic sediments, with thicknesses reaching up to 3.5 km. The Lalaye-Lubine-Baden-Baden shearing corresponds to the limit between the Saxothuringian domain and the Moldanubian domain in the URG. The Badenweiler-Lenzkirch shear zone delimits the intra-Moldanubian domain (Krohe and Eisbacher 1988).

The URG has undergone multiple phases of deformation since the Variscan orogeny. It began with a northward compression, forming NW and NE shear faults, followed by an NNE extension reactivating NW to WNW oriented faults until the Permian. Subsequent NE compression and thrusting during the Permian were associated with NW and E trending shear faults. Late Permian extension created basins along NE to ENE structures (Fig. 1b; Villemin and Bergerat 1987; Schumacher 2002; Ziegler et al. 2006), while NE to NNE granitoid intrusions affected Carboniferous and Permian terranes (Lagarde et al. 1992; Altherr et al. 1999, 2000; Edel and Schulmann 2009).

Bundsandstein (sandstones), Muschelkalk (limestones), and Keuper evaporites filled the URG during the Triassic (Sittler 1985), followed by Jurassic carbonate deposition in an overall extensional phase. Due to the uplift and erosion from the Late Jurassic to Early Eocene, no evidence of Cretaceous sediment remained (Schumacher 2002).

Formation of the URG was initiated in the Early Eocene under the N Alpine compression, reactivating ENE and NNE faults (Ziegler 1992; Schumacher 2002). Late Eocene to Early Oligocene E to WNW extension was influenced by thermal anomalies and resulted in a thinner crust (Illies et al. 1967; Ziegler and Dèzes 2005), generating NNE faults (Illies and Greiner 1979; Schumacher 2002). Late Oligocene NE compression reactivated the URG border faults (Villemin and Bergerat 1987; Schumacher 2002), while Miocene NE and NW compressions transformed the URG into a shear zone and reactivated N and NE faults under ongoing Alpine push (Illies and Greiner 1979; Bergerat 1985; Edel et al. 2006; Rotstein and Schaming 2011).

The current maximum horizontal stress within the URG is NW-oriented (Heidbach et al. 2016). However, the faulting regime varies across the URG: in the northern part, active normal faulting dominates within an extensional setting, while the southern URG is characterized by a predominantly strike-slip faulting regime (Larroque et al. 1987; Cuenot et al. 2006; Meixner et al. 2014). Seismic activities

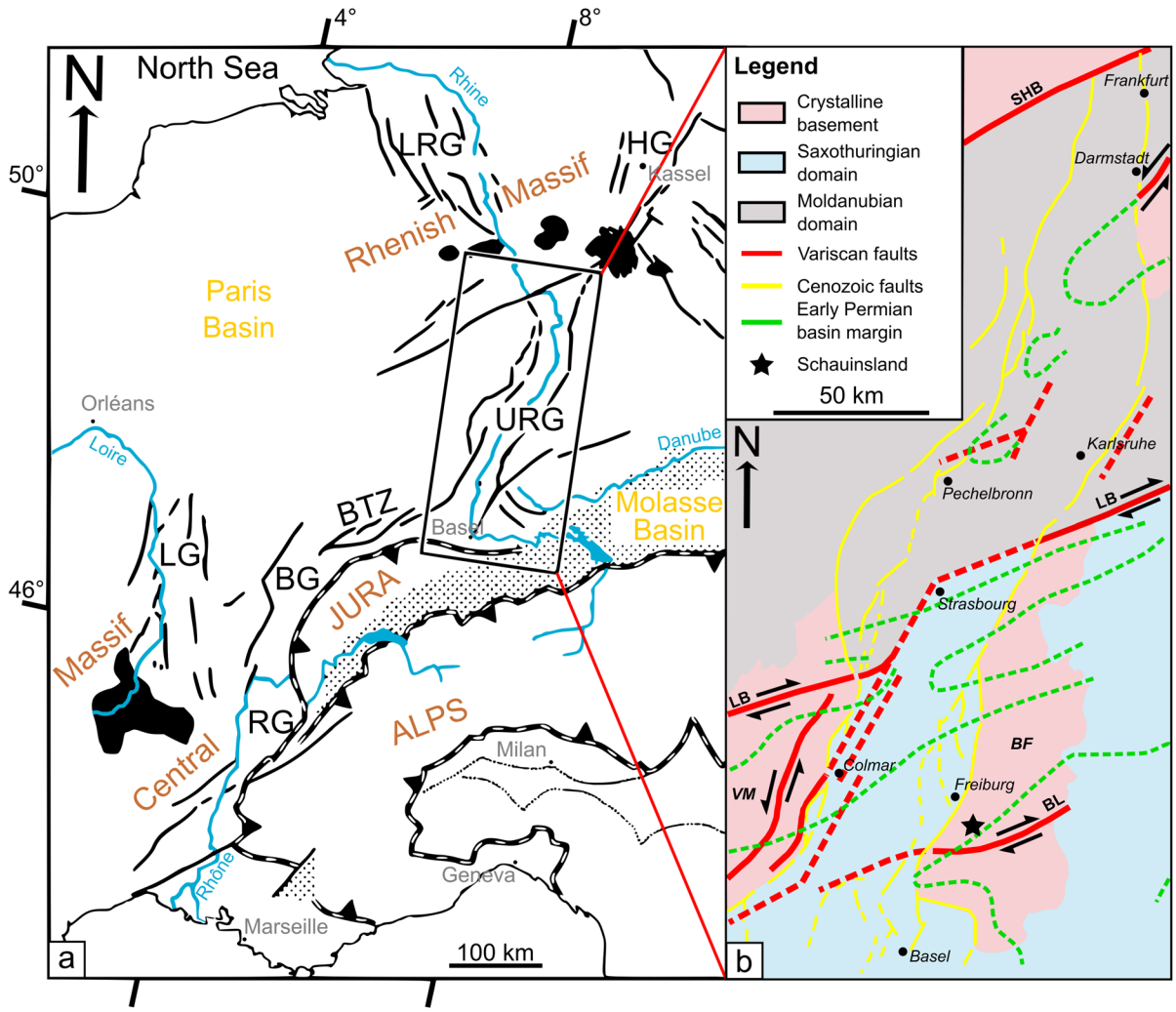

Fig. 1 **a** Simplified structural map of the European Cenozoic rift system modified after Schumacher (2002). Main European structural units are represented with dark lines. Cenozoic volcanics are represented by the dark spots and alpine Molasse by the dotted zone. BG, Bresse Graben; BTZ, Burgundy Transform Zone; HG, Hessian Grabens; LG, Limagne Graben; LRG, Lower Rhine Graben; RG, Rhône Graben; URG, Upper Rhine Graben. The rectangle indicates the zoom on the Upper Rhine Graben. **b** Upper Rhine Graben structural map modified after Schumacher (2002). Shearing is indicated by the dark arrows. The star indicates Schauinsland location. BF, Black Forest; BL, Badenweiler-Lenzkirch zone; LB, Lalaye-Lubine-Baden-Baden Fault; SHB, South Hunsrück-Taunus border fault; VM, Vosges Massif

with magnitudes ranging from 1.1 to 4.1, including natural and induced events, are recorded within the URG (Doubre et al. 2022). Natural seismic events are related to the reactivation of pre-existing structures within the URG while induced events are linked to geothermal activities such as in Vendenheim (Schmittbuhl et al. 2022).

The Black Forest forms the eastern shoulder of the URG (Fig. 1b). It is partly overlain by Permian arkoses and conglomerates, Triassic quarzitic sandstones, limestones, shales, evaporites, and clastic sediments, as well as Jurassic carbonates and clastic sediments (Geyer et al. 2011). The crystalline basement of the Black Forest comprises magmatic and metamorphic rocks. Paragneiss, orthogneiss, granodiorites, metabasites, peridotites, pyroxenites, granulites, and leucocratic gneisses are outcropping and dated to the Early Paleozoic (Altherr et al.

2021). The black star on the structural map represents the location of the Schauinsland Mine which is described in detail in Fig. 2 (Fig. 1b).

Seismic activity continues in the area of the Black Forest, with recent events in its central part having magnitudes of 3.1 in 1979 and 4.4 in 2002. These events revealed a hypocenter alignment at a depth of 11 km, oriented in a WNW-ESE direction (Häge and Joswig 2009; Doubre et al. 2022).

The Schauinsland massif in the Black Forest, historically mined for galena, sphalerite, and silver, is predominantly composed of gneiss (Wittenbrink 1999). Variscan deformation structures are accessible within the mine galleries and offer a 3D view of fault zones resulting from the reactivation of inherited structures. These fault zones comprise the E-W Variscan thrust (Fig. 2a) and NNE-SSW granitic intrusions formed through dextral shearing (Fig. 2b). The Variscan thrust was reactivated from the Lower Jurassic to the Lower Cretaceous, and led to the formation of a clay-rich shear zone with evidence of cataclasitic deformation (Werner et al. 2002; Fig. 2c). This fault zone was sheared in dextral direction through the Cenozoic with the reactivation of NNE-SSW structures, leading to ore vein formations (Fig. 2d).

The Ruschel Fault Zone (RFZ) corresponds to a WNW-oriented clay-rich shear zone, approximately 35 m long, which can be observed in a NNE-striking mine gallery (Fig. 3). It shows evidence of cataclasite, illitization related to tectonic reactivations, hydrothermal alteration, and plastic deformation associated with N-oriented dextral transtensive faulting from the Late Oligocene to the Miocene (Werner et al. 2002; Rotstein and Schaming 2011). The RFZ is described as a multi-core shear zone (Choi et al. 2016; Avakian et al. 2025) within a gneissic host rock. The

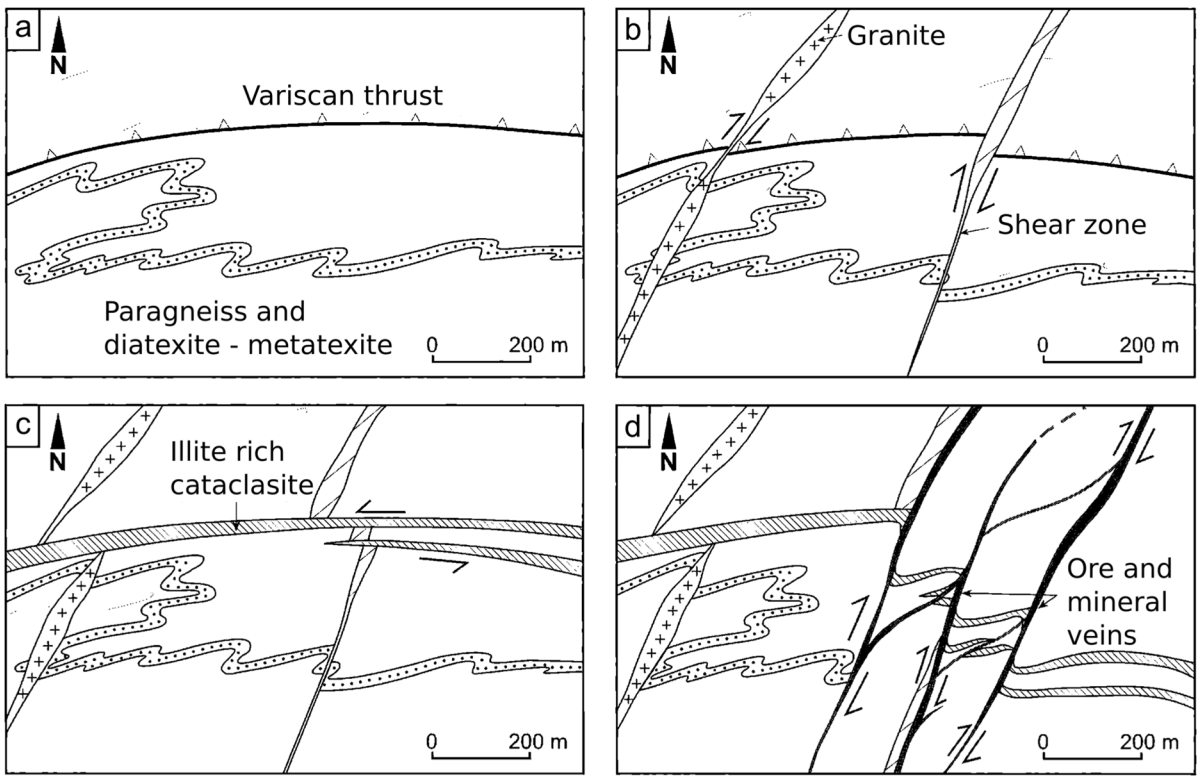

Fig. 2 Tectonic evolution and structural inheritance of the Schauinsland massif since the Variscan orogenesis (location is a black star in Fig. 1). **a** Inherited Variscan thrust in a metamorphic basement from the Upper Carboniferous. **b** Granitic intrusion and dextral shearing from the Upper Carboniferous to the Permian. **c** E-W shearing and reactivation of the inherited Variscan thrust from the Jurassic to the Cretaceous. Development of a clay-rich shear zone with evidence of cataclastic deformation and illitization. **d** Ore vein formation along with the shearing of NNE-SSW inherited structures during the Cenozoic. Modified after Werner et al. (2002)

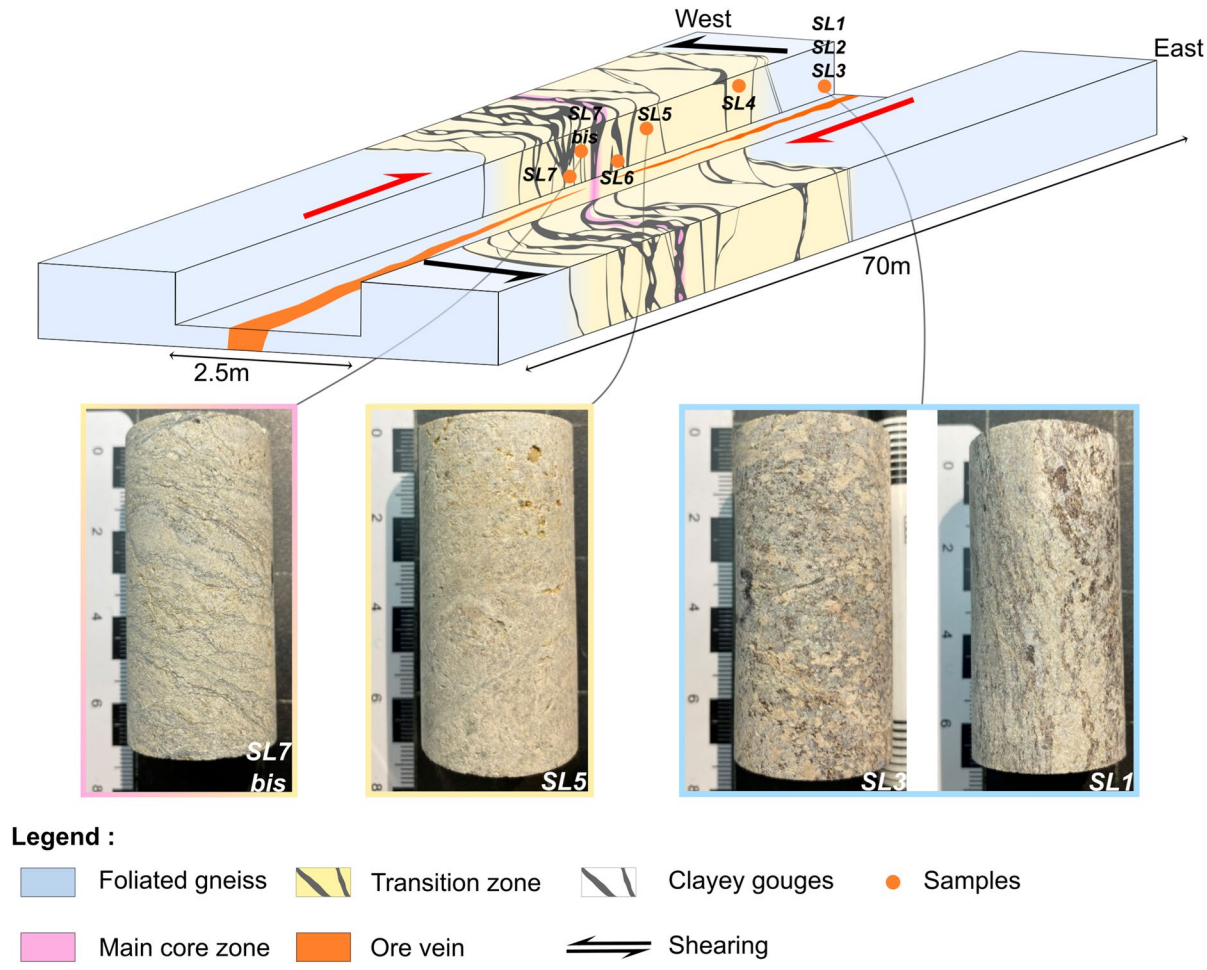

Fig. 3 3D conceptual scheme of the Schauinsland Mine, illustrating the multi-core architecture of the RFZ, characterized by the succession of multiple clayey gouges within the transition zone (modified after Avakian et al. 2025). Analyzed core samples are indicated by the orange dots. Shearing directions are represented by the black and red arrows. Below the 3D scheme, pictures of cored samples are displayed with color indicating their origin: blue for the host rock, yellow for the transition zone, and yellow/pink for the area next to the main core zone

alternation between sub-vertical clayey gouges and hydrothermally altered and deformed gneiss is observed in the transition zone (TZ) of the RFZ (Fig. 3). The largest clayey gouge, approximately 1 m in width, is found in the center of the RFZ and is interpreted as the main core zone of the structure (Avakian et al. 2025). A NNE-striking hydraulic breccia rich in quartz, sphalerite, galena, barite, and carbonate is visible on the roof of the gallery. It results from hydrothermal fluid flow during the N-oriented deformation of the RFZ. This breccia corresponds to an exploited ore vein and is only visible in the gneiss and the TZ of the RFZ (Fig. 3).

The interaction between the RFZ and the intersecting ore vein is considered an analogue to the fractured crystalline geothermal reservoirs of the URG where the Black Forest is a shoulder of the graben, providing access to outcropping kilometer-deep basement rocks (Figs. 2,3). Moreover, the NNE and WNW fault orientations in the Schauinsland Mine are similar to those encountered within the URG geothermal reservoirs (Glaas et al. 2021). The ore vein is considered an analogue of a tectonic structure in which present-day brine circulation would occur when it encounters a clay-rich shear zone.

Geomechanical investigations were carried out to better document whether and how the changes in lithology within the RFZ may have influenced the formation of the ore vein and pre-conditioned subsequent fluid circulation. This is of major importance for geothermal exploitation as fault zones and subsequent damage zones are targeted as main fluid pathways, such as in the Rittershoffen geothermal site (Glaas et al. 2021).

3 Materials and methods

In the following sections, the sample material is first described, followed by the experimental designs and conditions.

3.1 Material

Samples were collected from the Schauinsland Mine in the Black Forest (Germany) by extracting unoriented blocks across the RFZ exposed in a mine gallery. Sampling focused on three different zones: the host rock, the transition zone, and the area next to the main core zone. Host rock samples were obtained furthest from the main core zone to minimize the influence of hydrothermal alteration and deformation associated with the RFZ. The transition zone exhibited evidence of hydrothermal alteration, removal of the foliation, and a change in fabric compared to the host rock, but without clayey gouges. The main core zone is composed of meter-scale clayey gouges, underlining the multi-core architecture of the RFZ. The extracted blocks were prepared and cored in laboratory facilities for experimental testing. Notably, sampling from the main core zone was not feasible due to the non-cohesive character of the clayey gouges, which fragmented upon extraction. As a result, the mechanical properties of the main core zone could not be evaluated at the intended sample size due to the limitations encountered during sampling. The samples from the three different zones of the RFZ exhibited significant differences in composition and texture. The mineral content of the host rock samples was determined with Diffuse Reflectance Infrared Fourier Transform Spectroscopy (DRIFTS), following the procedure described in Avakian et al. (2025). Measurements were taken in the infrared range of 375 to 4000 cm^{-1} with 90 scans per sample (Herron et al. 2014). It should be noted that the DRIFTS measurements cannot quantify biotite content reliably due to limitations of the method. Biotite has to be detected with other methods, such as thin section analysis. The same method was applied to samples from the transition and those next to the main core zone, with data modified after Avakian et al. (2025) (Figs. 3, 4). Furthermore, illite was previously identified in Avakian et al. (2025).

The host rock, a foliated gneiss, exhibits macroscopically visible foliation, as represented by the samples SL1, SL2 and SL3. DRIFTS measurements indicate that these samples contain approximately 50–60% quartz and feldspar, followed by 14–19% illite, 5–8% smectite, and approximately 3–5% each of calcite and dolomite. The samples also contain approximately 4–6% kaolinite, 2–3% chlorite, and minor amounts (< 1%) of muscovite (Fig. 2). The transition zone, represented by samples SL4 and SL5, exhibits a foliation in various directions, though it is much less pronounced than in the host rock. The mineral composition includes 51–53% quartz and feldspar, ~ 9–17% illite, ~ 7–13% each of dolomite and calcite, ~ 6–12% kaolinite, ~ 2–7% smectite and ~ 4–5% chlorite. Samples SL6, SL7 and SL7bis, collected next to the main core zone, contain clayey gouges with varied orientations and frequent breakouts. Their mineral content consists of 33–41% quartz and feldspar, ~ 21–24% illite, ~ 13–17% kaolinite, and ~ 5–8% each of calcite, dolomite, chlorite, and smectite.

3.2 Experimental design and conditions

The experimental designs of the different test types are described below, starting with the mechanical apparatus and followed by the porosity and permeability setups. All mechanical experiments, gas permeameter, and mercury porosimeter measurements were done at GFZ (Germany). Petrographical observations were executed at CY Cergy Paris Université (France).

3.2.1 Mechanical tests

The tests were performed in a Mechanical Testing System (MTS) 815 triaxial compression cell (Fig. 5). The MTS is a servo-controlled compressive testing machine with a rigid, servo-controlled

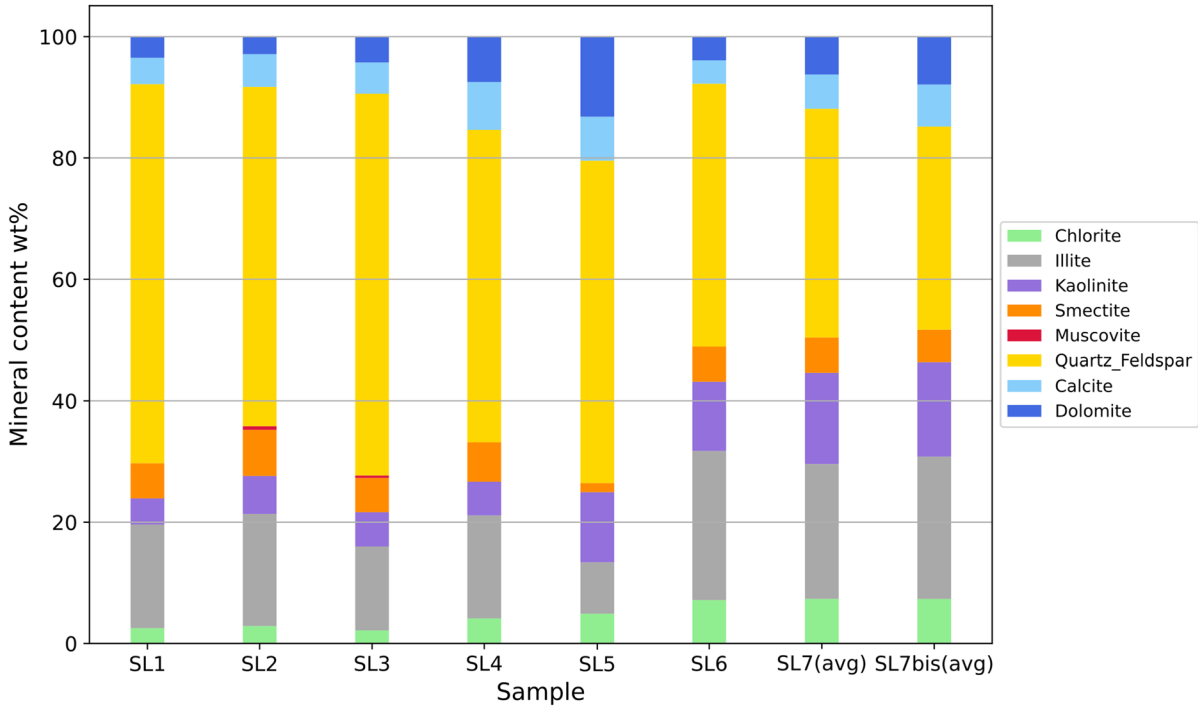

Fig. 4 Mineral content determined through a pre-analysis using Diffuse Reflectance Infrared Fourier Transform Spectroscopy. Samples SL1, SL2 and SL3 represent the host rock, while SL4 and SL5 are from the transition zone. Samples SL6, SL7, and SL7bis were taken next to the main core zone. The average mineralogical composition of SL7(avg) and SL7bis was calculated from multiple sub-samples and is shown in the figure. Data for the transition zone and the samples next to the main core zone have been modified after Avakian et al. (2025)

load frame. Compression forces up to 4600 kN and tension forces up to 2300 kN can be exerted. The load cell is calibrated to 1000 kN and has an accuracy of 0.1 to 1%, resulting in a systematic error of ± 1 to 10 kN for each measurement. In addition, a servo-controlled hydraulic confining pressure of up to 140 MPa can be imposed in an oil-filled pressure vessel, coupled to an external pressure intensifier. Strain was measured using a circumferential LVDT extensometer and two axial LVDT extensometers (Pei et al. 2018). All tests were carried out at room temperature.

Cylindrical samples for mechanical analysis were drilled from collected blocks in the direction of the main stress axis (or perpendicularly to pre-existing features such as foliation, fractures, or clayey gouges). Afterward, the samples were cut and dried at 60 °C for 24 h before the experiments began. The sample diameter was limited to 30 mm because of size limitations of the sample blocks to be transported out of the mine.

Tensile strength experiments were conducted according to the Brazilian tensile test with two curved jaws (Fig. 5c), in which the sample was placed. The sample size is 30 mm in diameter and 15 mm in length. The constant displacement rate was set to 0.001 mm·s^{-1} with a standard deviation of 3.0 to 6.0·10^{-4} mm s^{-1}. Afterward, the samples were placed in the apparatus and loaded either perpendicular to the foliation or to an approximate angle of 45°. In some samples, the foliation exhibited various directions, which caused variation in the loading direction relative to the foliation. In total, 49 samples were investigated. Three parameters were calculated from the Brazilian tensile test: the tensile strength T_0, the cohesion S_0, and the fracture toughness mode 1 K_{IC}.

The tensile strength T_0 was calculated as followed:

$$T_0 = \frac{2F_{max}}{\pi dl} \quad (1)$$

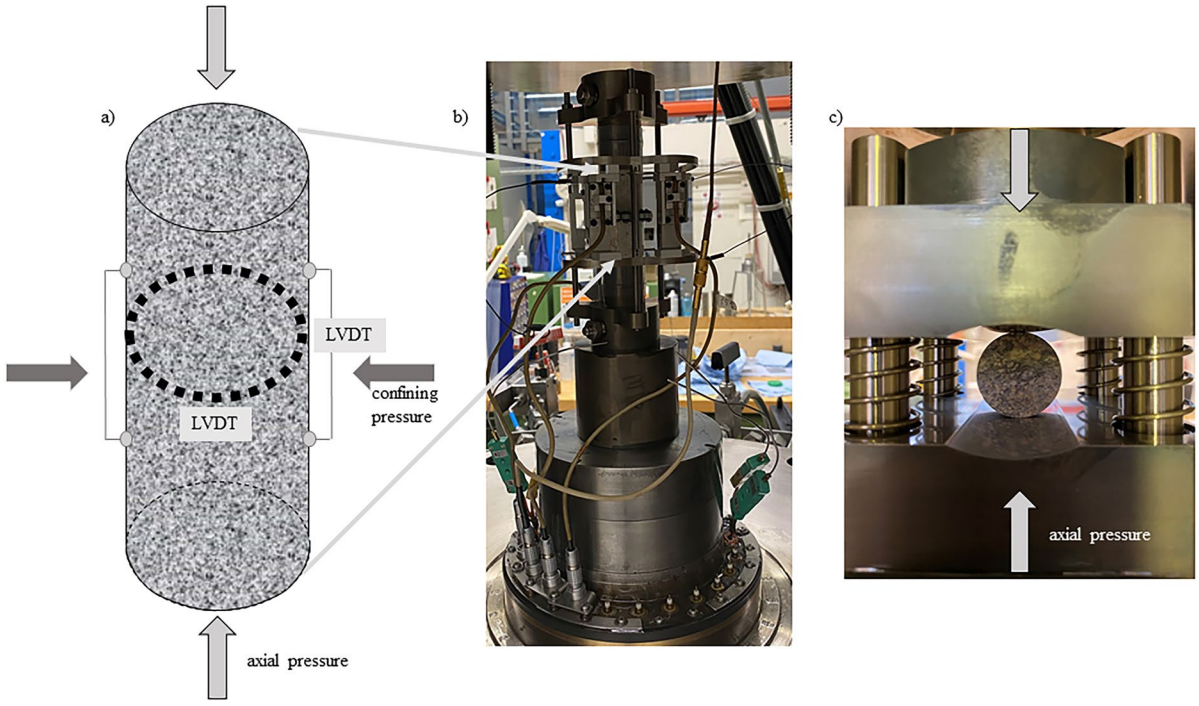

Fig. 5 Sample setups for the MTS experiments presenting, **a** the uniaxial and triaxial compressive strength test, **b** implementation in the triaxial cell and **c** Brazilian tensile test (modified after Kluge et al. 2021)

with d = diameter, l = length and F_{max} = applied load at the local maximum (Fairhurst 1964; Peng and Zhang 2007, Chap. 4; Li and Wong 2013).

The cohesion is estimated based on the Griffith criterion (Griffith 1924; Peacock et al. 2021) by considering $\sigma'_n = 0$. It is given by:

$$\tau = S_0 = 2T_0 \tag{2}$$

where τ is the shear stress, σ'_n = the normal stress, T_0 = tensile strength, and S_0 = cohesion.

The fracture toughness mode 1, $K_{IC,}$ is based on the measured stress and strain (Guo et al. 1993).

$$K_{IC} = \frac{2F_{min}}{\pi^{\frac{2}{3}}\left(\frac{D}{2}\right)^{0.5} l\theta}\Phi\left(\frac{c}{r}\right) \tag{3}$$

in which $\phi(c/r) = 0.112$ is the dimensionless stress intensity factor, $\theta = 3°$ contact angle, r = radius, l = disc thickness, F_{min} = applied load at the local minimum after failure, and D = diameter of the sample (Guo et al. 1993).

The uniaxial compressive strength (UCS) and triaxial compressive strength (Triax) tests were conducted using the following setup. The samples were surrounded by shrink tube and placed between two sample holders. The samples were 30 mm in diameter and 60 mm in length. The constant displacement rate was set to 0.001 mm·s^{-1}. During a uniaxial compressive strength test, Young's Modulus E, uniaxial compressive strength UCS and Poisson ratio υ were determined. The Young's Modulus and Poisson ratio were calculated for the interval from 40 to 60% of the maximum axial stress (ASTM International, 2014) (Supplementary Material Fig. 1, 2). In total, three samples were tested.

$$E = \frac{d\sigma}{d\varepsilon_a} \tag{4}$$

$$UCS = \frac{F}{A} = \frac{F_{max}}{\pi r_0^2} \tag{5}$$

$$-\varepsilon_l = -\frac{dD}{D}, \quad \varepsilon_a = \frac{dL}{L} \tag{6}$$

$$\upsilon = -\frac{\Delta\varepsilon_l}{\Delta\varepsilon_a} \tag{7}$$

with σ representing the stress, ε_l for elastic strain, ε_a for axial strain, D for diameter of the sample, F for applied force, F_{max} for applied force at the maximum before failure, A for the sample area, r_0 for the initial radius, and L for length of the sample (Jaeger et al. 2007, Chap. 4).

It should be noted that the sample material collected next to the main core zone was broken before the experiment began. Therefore, UCS results for theses samples are excluded from the study.

The individual Triax tests were performed at confining pressures of 20 MPa, 40 MPa, and 60 MPa. The confining pressure was applied with a constant stress rate of 0.5 MPa·min^{-1}. Subsequently, the axial displacement was gradually increased with a rate of 0.001 mm·s^{-1} until failure of the sample. In total, eight samples were investigated. Additionally, two multiple failures were induced by a stepwise increase in confining pressure. The first confining pressure ramp level was set to 20 MPa. Then, axial loading was applied until the onset of yielding. After stopping the axial loading, the confining pressure was increased to 40 MPa, and axial loading was resumed again until the onset of yielding. At 60 MPa confining pressure, axial loading was continued until failure. This procedure required only one sample to achieve three different triaxial compressive strength values. The triaxial compressive strength test determines the Elastic Modulus E_{triax} and the peak stress σ_{peak} (Eq. 8–11). The E_{triax} describes the nearly linear curve of the stress–strain behavior of the rock sample while loading and was calculated using a differential stress interval of 40 to 60% of the sample's peak strength (Eq. 11). The σ_{peak} is determined by the differential stress σ_{diff}, at the point of failure, describing the peak strength of the sample. During testing at the MTS, the confining pressure P_c and axial displacement rate were applied, and the axial force F_a was measured. The confining pressure is compensated with this read out. Confining pressure P_c was applied with hydraulic oil ($\sigma_2 = \sigma_3$). Therefore, we can calculate the differential stress directly from the data as follows:

$$\sigma_{diff} = \frac{F_a}{\pi r_0^2} \tag{8}$$

With σ_{diff} = differential stress, r_0 = initial radius of the sample, and F_a = axial force.

According to Terzaghi (1925) the axial stress (maximum principal stress) can be calculated as follows:

$$\sigma_1 = P_C + \sigma_{diff} \tag{9}$$

The peak stress was determined at the point of failure of maximum differential stress:

$$\sigma_{peak} = \sigma_{diff,max} \tag{10}$$

To allow for comparison with other studies, the initial radius r_0 of the sample of the intact samples was used for calculation of the peak stress.

The Elastic Modulus was calculated from the change in differential stress to the change in axial strain $\varepsilon_{a,\,triax}$.

$$E_{triax} = \frac{d\sigma_{diff}}{d\varepsilon_{a,triax}} \tag{11}$$

in which σ_{diff} = differential stress and $\varepsilon_{a,\,triax}$ = axial strain of the triaxial experiment.

As confining pressure increases, the rock can undergo large strain while holding the load (further increase in axial stress). The yield point is passed when the strain rate increases significantly with loading (Jaeger et al. 2007). Then, the rock failure shifts from brittle to brittle-ductile transitional failure. Ductile failure in triaxial experiments is defined as the ability of the rock sample to deform under load, in contrast to brittle failure, which is characterized by decreasing strain when the rock cannot sustain the applied load (Jaeger et al. 2007, Chap. 4).

3.2.2 *Permeability and porosity tests*

The permeability was measured in a gas permeameter with argon. The setup consisted of a cylindrical sample with a diameter of 25 mm and a length of 50 mm. The sample was sealed with a neoprene tube on a plug made of hardened steel. The other side of the sample was positioned on a piston that closed the pressure vessel. A confining pressure of 25 bar was applied to ensure proper sealing of the setup. A pressure pulse of 20 bar

was applied to the inlet side of the sample. Meanwhile, the time was recorded until the gas reached the outlet side and equilibrium was established. The permeability was calculated according to Brace et al. (1968), where the pressure gradient decays exponentially over time. This is displayed in the sample decay curve. The calculations are as followed:

$$\alpha = \left(\frac{kA}{\mu\beta L}\right)\left(\frac{1}{V_1}+\frac{1}{V_2}\right) \tag{12}$$

$$\left[\frac{\beta_{eff}-\beta_s}{\beta}+\eta\left(1-\frac{\beta_s}{\beta}\right)\right]\left(\frac{\partial P}{\partial t}\right) \tag{13}$$

$$\Delta p = P_1 - P_f \tag{14}$$

in which α = slope of decay curve, μ = viscosity of fluid, $\beta = 1.0 \cdot 10^{-9}$ cm^2·dyne for the fluid compressibility from the experience of Brace et al. (1968), Δp = pressure decay, β_{eff} = effective compressibility of the rock (measured in a jacketed sample) and β_s = compressibility of the minerals based on literature data from Brace et al. (1968).

$\left(\frac{1}{V_1}+\frac{1}{V_2}\right) = 1.12 \cdot 10^5$ 1·m^{-3} represents the total argon reservoir, and $\mu_{argon} = 0.000022733$ Pa·s is the viscosity of argon at 20 °C. The sample decay curve was plotted against the time and pressure decay on a semi log scale. (Brace et al. 1968).

Porosity was measured via a mercury porosimeter (Hg-Poro) using a few grams of sample material. In this method, mercury is forced into the pores by applied pressure. The pressure is continuously increased, and the resulting decrease in the volume of mercury in the sample holder represents the pore volume. Conversely, the penetration pressure is inversely proportional to the pore size. The method relies on the depressurization phenomenon, where surface tension forces resist the penetration of the mercury due to a contact angle greater than 90°. To overcome this oppositional operating force, the pressure applied to the mercury penetration must exceed the surface tension force. Therefore, the Washburn equation is applied. (Thermo Scientific, 2019):

$$r_{pore} = \frac{2\gamma cos(\theta)}{p_{corr}} \tag{15}$$

in which γ = surface tension of pure mercury (typically 0.48 N·m^{-1}), θ = contact angle of mercury with the sample (typically 140°), r_{pore} = pore radius (m), and p_{corr} = the corrected pressure (Thermo Scientific, 2019).

$$r_{pore} = \frac{0.735403}{p_{corr}} \tag{15.1}$$

The experimental setup of the mercury porosimeter consists of two instruments, operated under vacuum conditions. The first instrument, in which the sample is placed, operates at low pressure, with a maximum pressure of 400 kPa. It allows mercury to penetrate the mesopores. The second instrument, a high-pressure setup, has a maximum pressure of 400 MPa and is required to infiltrate the micropores. The output of the Hg-Poro consists of two data files, one file for each instrument. Both files were merged into the program SolidEvo, which calculates the required parameters, including porosity (Thermo Scientific, 2019). Porosity measurements using the triple weighing procedure presented in Avakian et al. (2025) were also applied on the host rock samples (SL1, SL2, and SL3).

4 Results

The results chapter is subdivided into the different research fields: petrography, geomechanics, porosity and permeability.

4.1 Petrographic observations

The gneiss (host rock) is composed of quartz, biotite, plagioclase, and K-feldspar, with a well-developed and deformed foliation (Fig. 6a). Evidence of hydrothermal alteration is observed through illite formation and quartz recrystallization. The filled fracture shown in Fig. 6b, which crosscuts the sample, contains quartz and carbonate.

The transition zone of the RFZ consists of a cataclasite resulting from shearing and hydrothermal alteration of the gneiss. The cataclasite contains fractured quartz, hydrothermally-altered plagioclase, biotite and K-feldspar (Fig. 6c, d). Fractures cutting through different minerals are filled with carbonates throughout the cataclasite. Locally, biotite has been

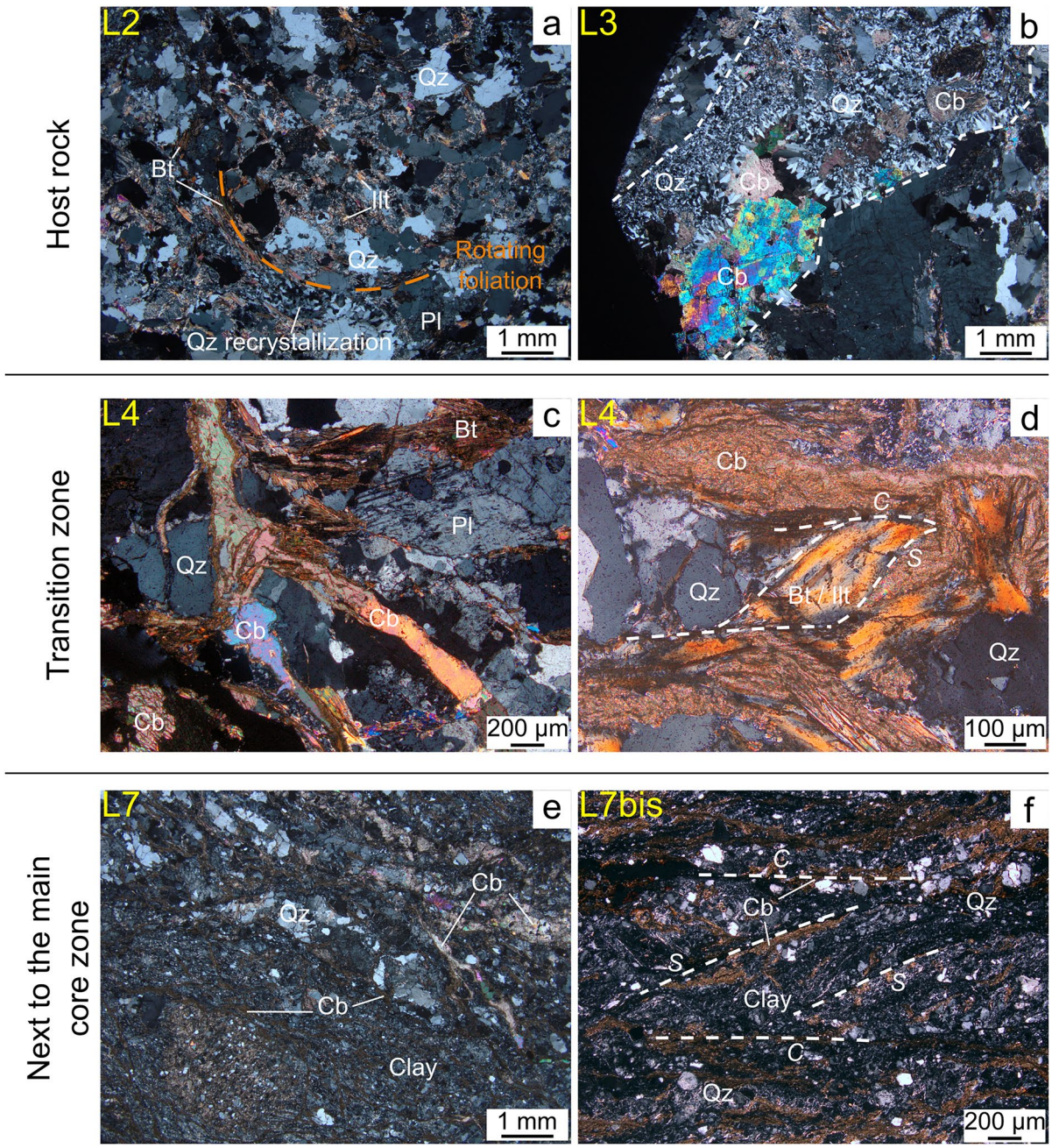

Fig. 6 Representative thin sections of the host rock, the transition zone and the cataclasite next to the main core zone. Sample names are indicated in yellow on each picture. **a** Gneiss in the host rock with a rotating foliation underlined in orange. Hydrothermally altered plagioclase, illite is observed along with quartz recrystallisation. **b** Gneiss in the host rock crosscut by a vein (bordered by the dashed lines) filled with quartz and carbonate. **c** Cataclasite from the transition zone containing fractures filled with calcite. **d** Deformed and hydrothermally-altered biotite in the cataclasite. The biotite lens is partially transformed into illite and shows S-C planes (white dotted S and C lines). Brownish carbonate surrounds the biotite lens. **e** Cataclasite enriched in clay minerals, with brownish carbonate veins and quartz. **f** Cataclasite composed of clayey gouges. The matrix consists of clay containing rounded quartz. Brownish carbonate and clay underline S-C planes. Thin section mineral abbreviations: Bt = biotite, Cal = calcite, Cb = carbonate, Ilt = illite, Pl = plagioclase, Qz = quartz, after Whitney and Evans (2010)

transformed into illite, resulting from its hydrothermal alteration (Fig. 6d). Biotite also exhibits a lens shape, highlighting the S-C planes formed by the RFZ shearing. Brownish carbonate veins following the S-C planes (Fig. 6f) display a dendritic pattern similar to those observed in granite by Duwiquet et al. (2021).

Cataclasites sampled next to the main core zone contain millimeter-sized clayey gouges (Fig. 6e), which themselves include crushed quartz grains and carbonate veins. Millimeter-sized quartz grains are mixed with micrometer-sized quartz grains, indicating grain size reduction compared to the host rock. Moreover, rounded quartz grains suggest shearing and associated cataclastic flow. The distribution of the different carbonate veins leads to anisotropy in the clayey gouges. Mineral lenses outlining S-C planes create structures that align preferentially in response to the RFZ shearing.

4.2 Mechanical behavior of fault zone rocks

Figure 7 summarizes the results of 49 samples from Brazilian tensile tests. Under loading perpendicular to the foliation, the host rock zone exhibits the highest tensile strength values, with a mean of 11.60 MPa. In contrast, samples next to the main core zone show the lowest tensile strength, with a mean of 4.95 MPa (Fig. 7, Table 1). This indicates a clear trend of decreasing tensile strength from the host rock to the main core zone.

Moreover, the results show a nearly linear relationship for the loading perpendicular and in various directions to the foliation, with an increase in tensile strength and fracture toughness mode 1 towards the host rock. However, loading oriented at 45° to the foliation exhibits a discontinuous trend. The results of the host rock tensile strength show from perpendicular to 45° oriented loading to the foliation, the greatest decrease in strength compared to the other zones. Moreover, for loading oriented at 45°, the fracture toughness mode 1 displays the highest value in the transition zone, intermediate value in the host rock, and the lowest value next to the main core zone. This establishes the transition zone as an outlier from the trend observed in the host rock towards the core zone.

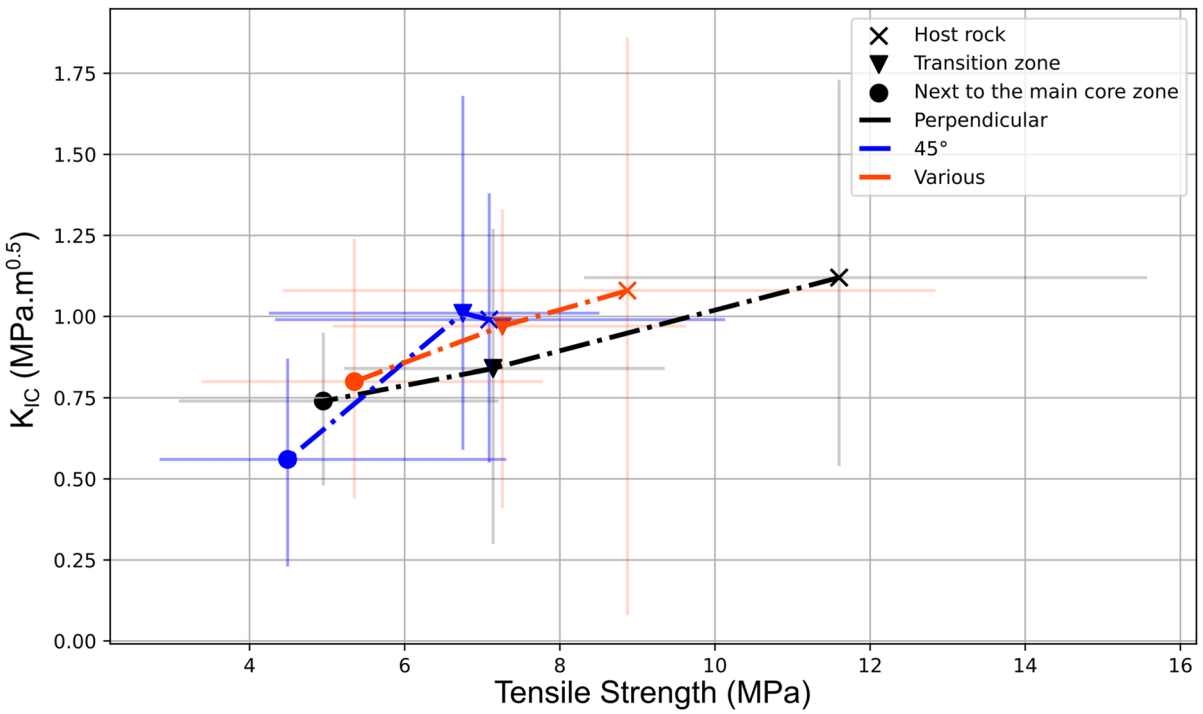

Fig. 7 Mechanical data of the tensile strength and fracture toughness mode I are presented in correlation to the anisotropy. The error bars correspond to the minimum and maximum values of each point

Table 1 Mechanical data of the tensile strength and fracture toughness mode I with N = number of samples

Zone	Loading direction to anisotropy	Tensile Strength (mean) (MPa)	Tensile Strength (Std.dev.) (MPa)	Cohesion (mean) (MPa)	K_{IC} (mean) ($MPa \cdot m^{0.5}$)	K_{IC} (Std.dev.) ($MPa \cdot m^{0.5}$)	N
Host-rock	Perpendicular	11.60	2.68	23.20	1.12	0.40	5
Transition	Perpendicular	7.14	1.22	14.28	0.84	0.30	9
Next to the main core zone	Perpendicular	4.95	1.32	9.90	0.74	0.16	5
Host-rock	45°	7.09	2.37	14.18	0.99	0.34	3
Transition	45°	6.75	1.59	13.50	1.01	0.36	6
Next to the main core zone	45°	4.49	1.58	8.98	0.56	0.21	5
Host-rock	Various	8.87	3.30	17.74	1.08	0.72	4
Transition	Various	7.26	1.44	14.52	0.97	0.28	7
Next to the main core zone	Various	5.35	1.81	10.71	0.80	0.27	5

Table 2 Mechanical data of the Young's Modulus and uniaxial compressive strength

Zones	Sample ID	E (GPa)	UCS (MPa)	υ (-)
Host-rock	SL1C	42.9	112.1	0.17
Host-rock	SL1B	41.0	96.4	0.20
Transition	SL5C	30.9	87.5	0.13

Table 2 summarizes the results of the UCS experiments on the samples collected across the RFZ. Three samples were evaluated: two from the host rock (SL1C and SL1B) and one from the transition zone (SL5C). The elastic modulus (E) and the uniaxial compressive strength (UCS) present higher values for the host rock than the transition zone, similar to the Poisson ratio.

The triaxial test results show that the E_{triax} exhibits the highest values, at 40 MPa confining pressure, across all zones. Preparation of the sample next to the main core zone, which was intended for the 60 MPa confining pressure experiment, was unsuccessful. The results show that the elasticity values are the lowest at 20 MPa, exhibiting a trend similar to that observed in the test conducted at 40 MPa confining pressure (decrease of elasticity from the host rock to next to the main core zone).

For $\sigma_{peak,}$ the sample next to the main core zone exhibits the highest strength values at 20 MPa confining pressure, reaching 169.2 MPa, while the host rock shows a lower value of 160.8 MPa. At 20 MPa confining pressure, the transition zone has the lowest σ_{peak} of all zones. At 40 MPa confining pressure, the host rock indicates the highest σ_{peak} (252.1 MPa), followed by the sample next to the main core zone (218.3 MPa). At 60 MPa, the host rock has the highest σ_{peak} with an average of 301.75 MPa, while the transition zone reached only 229.9 MPa (Table 3). The results indicate a linear trend of increasing σ_{peak} within each zone as confining pressure rises. Additionally, the E_{triax} decreases linearly from the host rock to the core zone across all confining pressure states.

Here, the results of the axial strain measurements from the triaxial compressive strength tests are evaluated. At a confining pressure of 20 MPa, the host rock displays brittle failure behavior (Fig. 8a). For the subsequent confining pressures of 40 MPa and 60 MPa, there is a slower decrease in stress after the failure, resulting in an axial strain of more than 0.01 before reaching 100 MPa differential stress. An exception is the multiple failure test, which shows axial strain values lower than 0.005. With the exception of the Triax test for 20 MPa confining pressure, all other tests follow the same linear trend in the load curve.

The transition zone portrays two sharp brittle failures (SL4B_20MPa and SL4C1_40MPa) and one (SL4C2_60MPa) that tends more toward ductile behavior. Hereby, the SL4C2_60, representing the 60 MPa confining pressure conditions, portrays a post-failure behavior with an increase in axial strain of more than 0.02 around 100 MPa differential stress. It has to be noted, that the SL4C2_60 indicates a potential yield point about 160 MPa differential stress. In contrast, the transition sample at 20 MPa confining pressure, SL4B_20, shows brittle failure with

Table 3 Triaxial compressive strength test with confining pressure of 20 MPa, 40 MPa and 60 MPa presenting E_{triax} and $\sigma_{peak} = \sigma_{(1,\,max)}$-$P_C$

Zones	Sample ID	E_{triax} (GPa)			$\sigma_{peak} = \sigma_{(1,\,max)}$-$P_C$ (MPa)		
Confining Pressure (MPa)		20	40	60	20	40	60
Host rock	SL2B	37.6			159.3		
	SL1C1		50.1			254.9	
	SL1C2			47.7			262.7
	SL2_Multi	47.3	-	-	160.8	290.9	340.8
Transition	SL4B	33.7			148.3		
	SL4C1		41.6			197.5	
	SL4C2			36.5			230.3
	SL4_Multi	31.7	-	-	148.9	187.2	229.5
Next to the main core zone	SL7bis1	18.1			169.2		
	SL7bis2		22.0			218.3	

minimal axial strain accumulation. The multiple failure sample presents a slow decrease in stress in the post failure curve, resulting in strain accumulation similar to the SL4C2_60MPa confining pressure experiment and a yield point of approximately 110 MPa differential stress.

The samples close to the main core zone show a tendency toward ductile behavior during the triaxial compressive strength test. At 40 MPa confining pressure (SL7bis2_40), the failure curve shows a prolonged hold time at high stress, resulting in a high axial strain value of 0.020 before the sample actually fails. The failure is sharp, and the differential stress decreases to 113 MPa. The second sample, SL7bis1_20, presents lower axial strain values than the previous sample, especially before reaching the yield point of 148 MPa differential stress. The failure is sharp but stops around 65 MPa differential stress, with axial strain increasing up to 0.014.

The failure behavior across different confining pressure states shows a shift from brittle to ductile failure, from the host rock towards close to the main core zone. Moreover, as confining pressure increases, the tendency toward ductile failure also increases. Comparing the peak strength values with the stress–strain curves reveals a positive linear trend with increasing confining pressure, suggesting a potential correlation between the ability to accumulate strain and the resistance to applied stress.

To assess the potential effects of anisotropy on the calculated parameters, a post-failure analysis was conducted on three samples used in the triaxial experiments. For this purpose, one sample from each zone was analyzed in detail (Fig. 9). Figure 9a shows the host rock, where the sample contains a preexisting filled vein and foliation, highlighted both by biotite minerals that are diagonal to the end face, at an approximate angle of 20° to the longitudinal axis. The developed fracture partly follows the foliation, then deviates and cuts approximately two-thirds of the total sample length. Notably, the newly developed fractures do not follow the preexisting filled vein, suggesting a higher strength of the filling material.

The transition sample in Fig. 9b shows a foliation angle of approximately 40° to the longitudinal axis. Additionally, the foliation vanishes due to hydrothermal alteration and deformation phenomena. In this zone, the fracture follows the foliation along the sample. For the core sample (Fig. 9c), the foliation disappeared, and existing planes are now thin clayey gouges observable as grey layers. The clayey gouges show various directions, and preexisting filled fractures were also observed. The fractures either crosscut the clayey gouges or follow them briefly, depending on the orientation of the clayey gouges. In the less hydrothermally-altered areas of the core sample, the preexisting fractures remained unaffected, possibly due to the fracture-filling minerals, which may be similar to those in the vein of the host rock sample. Furthermore, the host-rock and samples close to the main core zone exhibit small foliation angles, leading to more vertical fractures than the transition zone. The end caps of the experimental setup may influence fracture development due to the small dimension of the sample (30 mm in diameter and 60 mm in length).

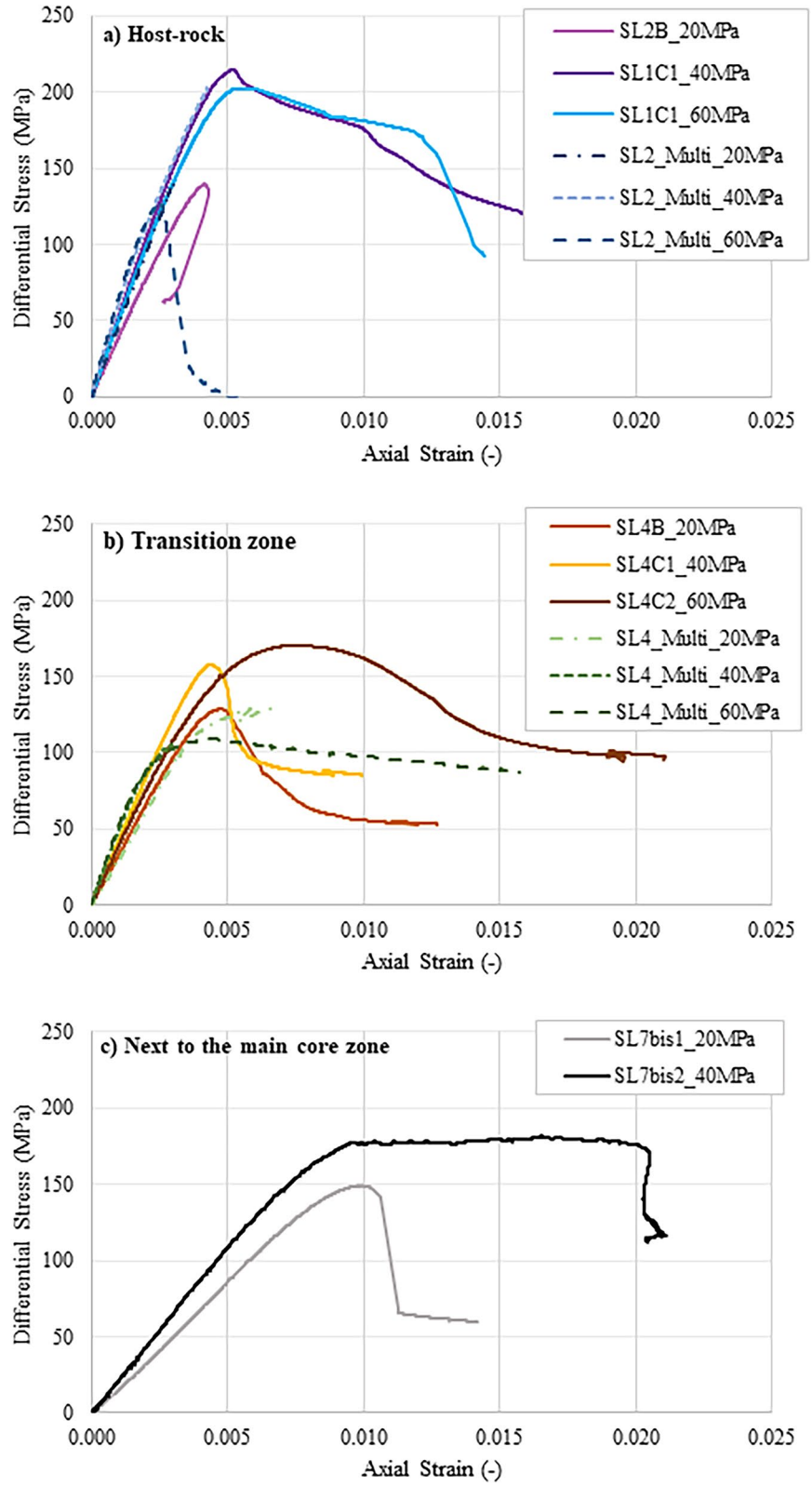

Fig. 8 Triaxial compressive strength test with confining pressure of 20 MPa, 40 MPa and 60 MPa. **a** Triaxial test of the host rock, **b** triaxial test of the transition zone and **c** triaxial test of the samples collected next to the main core zone

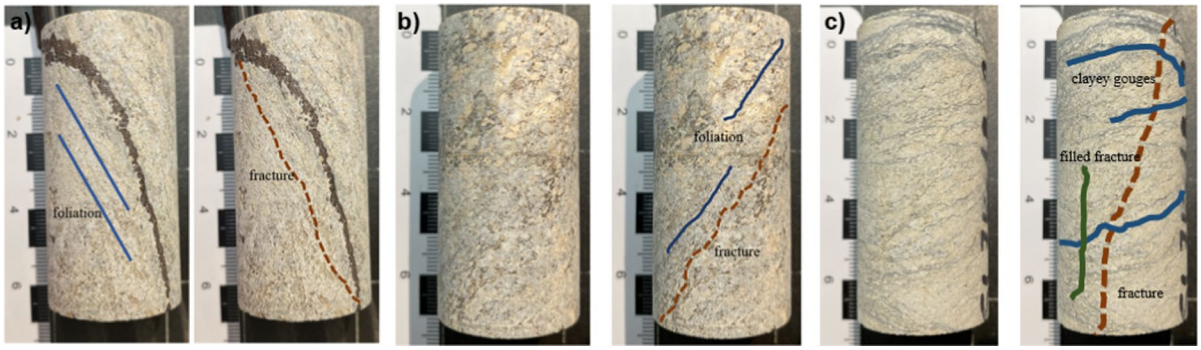

Fig. 9 Triaxial compressive strength test samples for the post failure analysis of **a** SL1C1_2 (20 MPa confining pressure), **b** SL4C_5 (40 MPa confining pressure), and **c** SL7bis1B_2 (20 MPa confining pressure). Green lines present preexisting filled veins, the brown dotted line is the fracture and blue lines highlight the foliation or clayey gouges

The mechanical behavior of the RFZ samples display a decreasing trend in strength from the host rock to the transition zone. This trend is similar for both the K_{IC} and the E_{triax} but extends until next to the main core zone. The results for σ_{peak} and subsequent strain behavior indicate that close to the main core zone samples exhibit greater strain accumulation throughout the test duration, along with higher σ_{peak} values compared to those from the transition zone. Furthermore, the post-failure analysis provides insights into the influence of foliation on fracture development and specimen stress resistance. After demonstrating the effects of rock composition on the mechanical behavior in fault zones, the question arises as to whether geothermal utilization would be sustainable due to the partially ductile behavior. Therefore, the permeability and porosity of the different zones must be examined to assess the potential liquid flow pathways.

4.3 Porosity–Permeability evolution

Figure 10 portrays the results of the porosity and permeability measurements of the different zones. Hereby, the porosity measurements from the Hg-porosimeter, along with data from Avakian et al. (2025), as well as the permeability measurements by a gas permeameter, are evaluated (Table 4).

The permeability measurements show a small range of permeability variation across the different zones. Porosity reveals for the transition zone values ranging from 1.51 to 3.57%. The average porosity of 2.34% is higher than that of the host rock, which has a mean of 1.67%. The core zone shows higher values, with a mean of 4.37%. Values from Avakian et al. (2025), using the triple weighing method, give much higher porosity values for the samples next to the main core zone (Table 4). A general trend of higher porosity values towards the main core zone is observed for both methods. However, the samples are highly heterogeneous, with some containing millimeter-sized veins in both the host rock and transition zone. These heterogenous characteristics were also noted in Avakian et al. (2025). Additionally, the samples enriched in clay have a finer grain size compared to those in the gneiss of the host rock (Avakian et al. 2025). Thus, the porosity and permeability measurements should be interpreted carefully, as these features may substantially impact the presented results.

Correlations between the clay content of the samples grouped by zone, porosity, and permeability are shown in Fig. 10. The host rock and transition zone present similar clay content and porosity values, based on Hg-intrusion measurements. The porosity data from Avakian et al. (2025) are included separately. Significant variations are observed in the samples next to the main core zone (Fig. 10), where the clay content increases by ~ 20% and the porosity increases by ~ 5%. The clay content and the porosity appear to be positively correlated. Both porosity measurement methods show a consistent trend of increasing porosity from the host rock towards the main core zone. Furthermore, clay content and porosity increase while permeability decreases (Fig. 10). However, the permeability range is narrow, varying

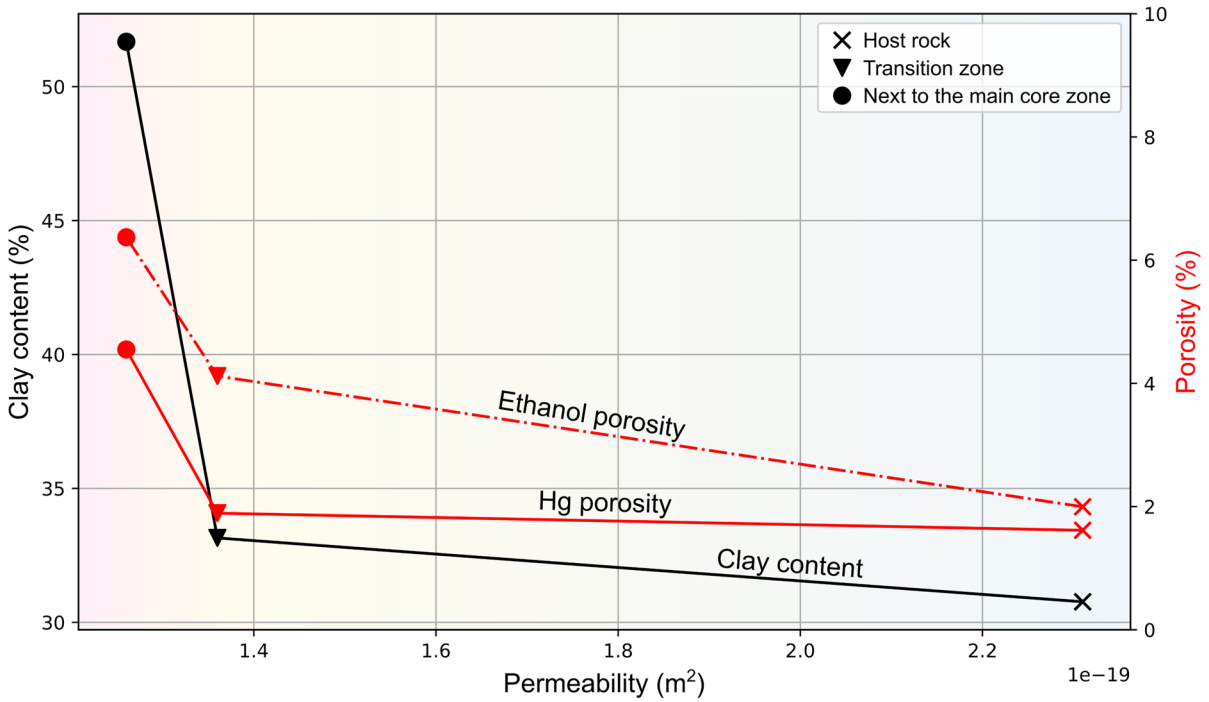

Fig. 10 Evolution of the clay content (%) and the porosity (%) with the measured permeability (m^2) per zone (host rock, transition zone and next to the main core zone). The permeability varying with the clay content (%) is represented in black. The permeability changing with the Hg-porosity (%) is shown by the red line. The dashed red line corresponds to porosity measurements obtained using the triple weighing method and modified data from Avakian et al. (2025). The background gradient shows the shift from the host rock (blue) towards the main core zone (pink)

Table 4 Porosity and Permeability dataset measured at GFZ and porosity data from Avakian et al. (2025)

Zone	ID	Porosity by Hg-intrusion			Ethanol porosity (Avakian et al. 2025)			Permeability		
		Mean (%)	Std. dev. (%)	Count	Mean (%)	Std. dev. (%)	Count	Mean (m^2)	Std. dev. (m^2)	Count
Host-rock	SL1	1.37	0.13	2	1.62	0.74	3	1.05E-19	-	1
	SL2	1.28	-	1	1.84	0.73	3	3.35E-19	2.94E-19	2
	SL3	1.05	-	1	2.87	0.18	3	1.89E-19	2.05E-20	2
Transition	SL4	1.51	-	1	2.28	0.18	3	1.36E-19	8.52E-20	2
	SL5	2.01	-	1	3.57	0.88	3	-	-	-
Next to the main core zone	SL6	0.08	0.03	4	6.51	2.03	3	-	-	-
	SL7bis	2.29	-	1	6.81	1.41	6	1.26E-19	-	1
	SL7	3.82	-	1	6.72	1.79	8	-	-	-

only between ~ 1.2 and $2.4 \cdot 10^{-19}$ m^2. The permeability data, accounting for its associated measurement uncertainty, suggests a possible tendency in the observed behavior (assessment values).

5 Discussion

The discussion chapter is subdivided into the discussion of the results on the sample-scale, their applications on the multi-core architecture of the RFZ, the RFZ as a geothermal analogue and the limitations of the study.

5.1 Sample-scale mechanical properties of the fault zones

This study of the mechanical properties of a shear zone with three different zones revealed unique features for each zone (Fig. 11). The transition zone marks the interface between the host rock and the main core zone, characterized by cataclasites filled with altered phyllosilicates and intermediate porosity (Fig. 11). Moreover, the transition zone exhibits a transitional type of failure, also referred to as "softening" (Jaeger et al. 2007). The results indicated brittle failure in the transition zone, along with the first trends of inelastic strain. Additionally, the fracture patterns observed after the triaxial compressive strength tests revealed that cracks propagate either along or through the weak foliation bands. Consequently, failure likely initiates in the fractured minerals within the cataclasite, possibly propagating within the foliation, influenced by the hydrothermally-altered biotite, resulting in lower strength compared to the surrounding feldspar and quartz (Bai and Young 2020).

Unlike the transition zone, the host rock exhibits higher strength due to its lower phyllosilicate content, degree of hydrothermal alteration, and porosity. This results in brittle failure of the host rock, driven by the inherent brittleness of quartz (Agliardi et al. 2014; He et al. 2023). The triaxial compressive strength tests revealed that failure followed the illite

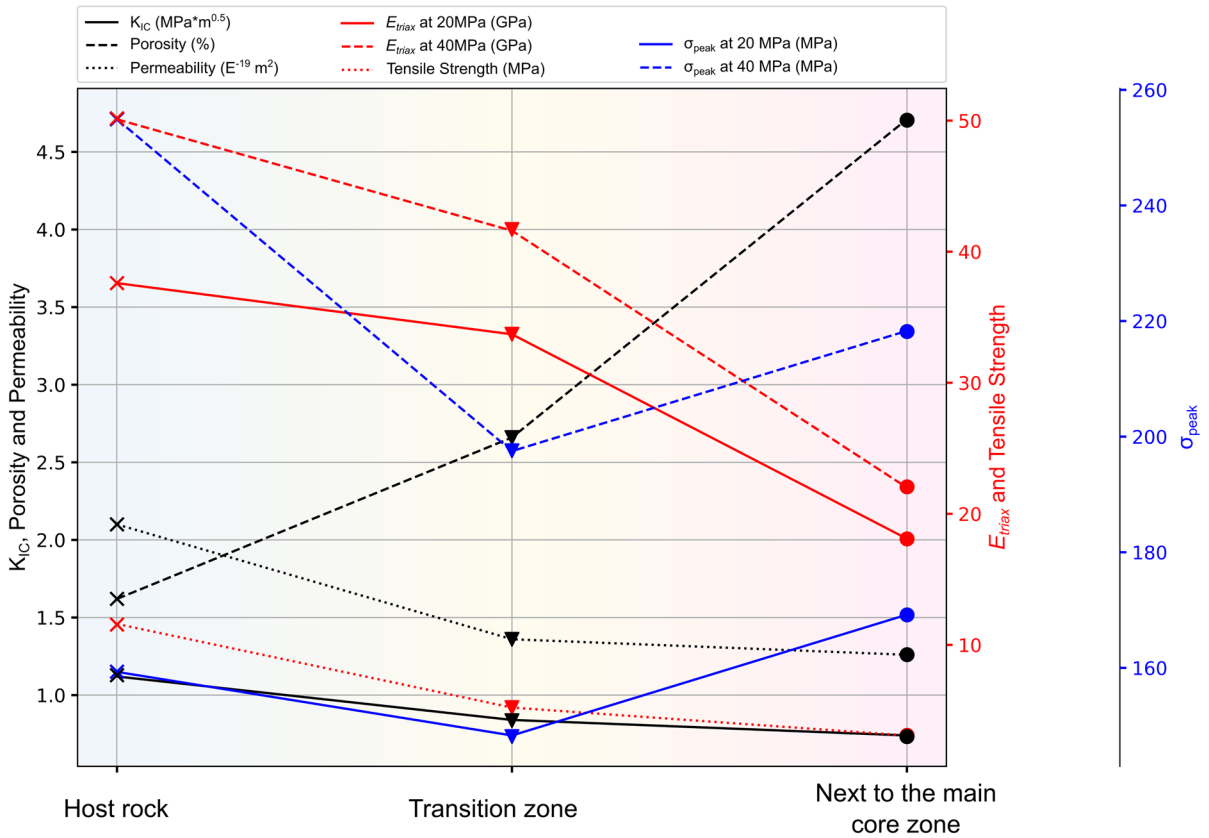

Fig. 11 Evolution of the rock characteristics from the host rock towards next to the main core zone. The color gradient underlines the transition between the different zones

and hydrothermally-altered plagioclase. This could be due to the lower stress resilience of illite and altered plagioclase compared to the surrounding quartz. Sajid et al. (2016) showed that recrystallization of fine-grained quartz or carbonate minerals, along with changes in textural characteristics due to alteration, leads to strengthening. This causes micro-cracks to propagate along the weaker planes rather than the recrystallized quartz or carbonate. Hence, the microstructure plays a critical role on the micromechanics of failure behavior, as mentioned by Agliardi et al. (2014).

For the samples next to the main core zone, petrographic observations revealed that mineralogical planes can consist of hydrothermally-altered biotite, clayey gouges containing illite and other clay minerals, or brownish carbonates. The degree of hydrothermal alteration, the number of S-C planes and porosity increased toward the main core zone (Avakian et al. 2025). The hydrothermal alteration indicates the dissolution of primary minerals, potentially increasing porosity. Therefore, fractured zones with high clay content indicate increased fluid flow, suggesting an indirect relationship between clay content and porosity. Fractures did not follow veins containing quartz and carbonate. Instead, the high quartz content increases stress resistance, causing fractures to develop along the clayey gouges. Clayey gouges act as planes of weakness due to their lower mechanical strength, but compaction and rearrangement of grains leads to high σ_{peak} values (Fig. 11).

5.2 Mechanical strength and cohesion variation with micro-structures and mineralogy

The fracture development is dependent on the angle of the foliation and clayey gouges. Towards the main core zone, the foliation angle increases and clayey gouges align more closely with the applied stress direction, especially in the transition zone (Fig. 9). Bai and Young (2020) found that when the foliation bands and the applied stress direction are not parallel, the sample strength can increase, which is consistent with the host rock samples (Table 3). In the samples next to the main core zone, fractures follow the S-C planes, highlighted by the mineral lenses, supporting high axial deformation rates. The high clay content, hydrothermally altered material and rounded quartz likely contribute to compaction, consolidation, grain rearrangement and interlocking of altered minerals which enhances higher stress resistance through plastic movement (Tenthorey and Cox 2006). Moreover, the reduction in grain size from the host rock toward the main core zone promotes steady-state sliding and results in high axial deformation rates next to the main core zone (Logan and Rauenzahn 1987). In contrast, the transition zone foliation angle and applied stress direction are closer, leading to minor sample strength.

The impact of heterogeneity of brittle rocks on the mechanical behavior exhibits grain-scale heterogeneities influencing the distribution of tensile stress and extensional crack development (Lan et al. 2010). Lan et al. (2010) suggest that heterogeneity is a primary factor controlling the stress–strain response, and an interpretation focusing solely on the peak strength is therefore insufficient. This aligns with the current study, which demonstrates a heterogenous composition of the sample material (clay, fractures, and foliation), leading to important mechanical and mineralogical contrasts within the RFZ. Next to the main core zone, samples might be more homogenous due to grain size reduction and the presence of gouge material. However, the lower tensile strength and therefore also lower cohesion values (Table 1) imply lower stability. Previous research has shown that the healing of microcracks increases fault zone cohesion (Tenthorey and Cox 2006), a phenomenon observed uniformly across all zones. However, the calculated cohesion values decrease from the host rock towards the main core zone which contrasts with the strength behavior. Potentially, the absence of clay gouges provided high cohesion values for the host rock while the opposite results in low cohesion values for the samples next to the main core zone. This is supported by the change in tensile strength in the host rock from perpendicular to 45° orientation. The strong reduction in strength could be related to the absence of clay gouges with their grain compaction and rearrangement potential. In addition to cohesion and tensile strength, the fracture toughness Mode 1 suggests that the samples next to the main core zone exhibit brittle characteristics, although they primarily display ductile failure behavior with minor residual brittle features. This interpretation is further supported by the post-failure analysis, which reveals a rapid decrease in differential stress after strain accumulation. Thus, cohesion, tensile strength and toughness show the importance

of the investigation of multiple parameters to prevent unrealistically optimistic interpretations of altered rock samples where mechanical parameters differ.

Based on the discussed parameters, two different mechanisms can contribute to high strength values (Fig. 11). First in the host rock, high quartz content, minimal hydrothermal alteration, foliation, and a heterogenous grain size distribution provide strong resistance against applied stress (Hofmann et al. 2015; He et al. 2023). Second, next to the main core zone, a high percentage of weathered biotite and feldspar, mixed clayey gouges, and increased porosity promotes plastic deformation and compaction. This results in grain rearrangement, which helps to restrain the applied stress (Wang et al. 1978; Logan and Rauenzahn 1987; Lu and He 2018; He et al. 2023).

5.3 Effects of mechanical properties on the multi-core architecture of the RFZ

Mechanical resistance differs across zones due to mineralogical variations and could be linked to the perpendicular ore vein formation (Figs. 2, 3; Werner et al. 2002; Pfaff et al. 2009; Avakian et al. 2025). The transition zone has the weakest resistance, transitioning from a brittle to ductile behavior. The host rock has the highest resistance, displaying purely brittle behavior. The main core zone undergoes stationary sliding with a ductile response. This contrast in mechanical behavior likely contributed to the opening of the ore vein structure in the host rock, where stresses could have accumulated.

Despite the presence of some clayey gouges, the transition zone opened due to its mechanical weakness. However, the main core zone remained closed, likely due to its high clay content, which acted as a stress-decoupling horizon. In this zone, clay minerals smeared rather than opening (Bedford et al. 2022). There may be a relationship between the width of the clayey gouges and their tendency to open through shearing or hydraulic brecciation (Faulkner and Rutter 2001). Only the main core zone contains a meter-wide clay gouge, whereas the smaller ones in the transition zone were crosscut.

In the gallery, we observed the ore vein crosscutting the vertical gouges and the foliation in the transition zone while in the post-triaxial image, we observed the fracture partly following and crosscutting the thin clayey gouges (Fig. 9c). Moreover, in large scale, we observed the clayey gouges going along the foliation and in small scale we observed fractures developing along the foliation. If the two-phenomena observed in the gallery and in the mechanical research are correlated, further investigations will be necessary to upscale the mechanical study from the sample to the structural scale.

5.4 RFZ mechanics as a geothermal analogue

Using the ore vein setting as an analogue for brine circulation within a crystalline geothermal reservoir implies that potential fluid flow may be possible in the transition zone of a clay-rich shear zone. The host rock has the lowest porosity values and clay content, resulting in less deformable space and material, whereas the samples next to the main core zone exhibits the opposite trend (Fig. 11). In contrast, permeability measurements indicate a low permeability across the investigated locations, with only a slight decrease next to the main core zone. Hydraulic stimulation could generate fractures that cut through the different zones of the RFZ, enhancing the fracture connectivity. However, only thin clayey gouges are likely to be opened for fluid flow, whereas meter-wide clay zones should be avoided to ensure reservoir connectivity. Hence, potential fractures induced by hydraulic stimulation may propagate along the foliation and partially along thin clay-rich gouge structures, rather than following the ore vein (Fig. 9a). Such stimulation could improve fluid flow rates for reservoir exploitation in crystalline rocks. However, the presence of mechanically weak, fine-grained minerals along the foliation may pose a risk of clogging. This also raises concerns about the potential for induced seismicity in response to hydraulic stimulation, particularly in relation to mineralogical and petrographic properties.

The study of the RFZ provides both mechanical and petrographic evidence for the influence of mineralogical heterogeneities on fault zone mechanical behavior. This coupling of deformation and hydrothermal alteration aligns with work by Dezayes et al. (2021), who similarly demonstrated these processes in geothermal fault zone formation and flow pathway evolution using surface analogue of the URG. Callahan et al. (2020) also coupled deformation and fluid/rock interactions to explain localized deformation or fault zone widening, applicable to geothermal

reservoir fault zones. Therefore, the mechanical and mineralogical properties of the RFZ likely induce complex fluid pathways that vary through time and space, as suggested by Klee et al. (2021b) in their study of the Noble Hills Range as a geothermal analogue. This is further supported by an underground research laboratory study (STIMTEC) in the Reiche Zeche mine in Freiberg, Germany, which indicated that the structural anisotropy and heterogeneity of the reservoir rock (strongly foliated metamorphic gneiss) had significant influence on the seismic activity from hydraulic stimulation tests (Boese et al. 2022).

Recognizing the geological complexity of the URG (Bauer et al. 2017), analogue sites provide valuable input for understanding key processes at depth within specific geological structures, particularly fluid-rock interactions and their evolution, depending on deformation amounts in transcurrent structures affecting the crystalline basement. To further investigate these processes in the crystalline basement of the URG, the GeoLaB underground research infrastructure, located on the granitic shoulder of the URG in SW Germany, will facilitate investigation of structural heterogeneities and their interplay with complex thermal–hydraulic-mechanical-chemical processes in fractured rocks (Bremer et al. 2025). Complementing this work, research at the Utah FORGE field laboratory (USA) focuses on addressing EGS-related challenges in crystalline rocks (Jones et al. 2024).

5.5 Limitations

Due to the small number of samples, the statistical power of our assumptions is limited, requiring additional experiments for verification. Another constraint is the sample size, as the mechanical behavior of rocks differs with scale. All mechanical experiments have been performed under dry conditions excluding saturation, fluid flow, and concomitant alteration of the host rock. Therefore, further testing at larger laboratory and field scales is necessary to investigate the interaction between mineralogy and mechanical parameters. Previous studies have shown contradictory results regarding the influence of the grain size (Tuğrul and Zarif 1999; Hofmann et al. 2015; Sajid et al. 2016; Saadat and Taheri 2019) and the effect of specific minerals on mechanical parameters (Sajid et al. 2016; Wong et al. 2018). These discrepancies highlight the strong dependence of the results on the investigated samples and rock types, making generalization difficult.

Nevertheless, the shear zone of the Schauinsland Mine can be divided into three sections with distinct mineralogical properties, each influencing mechanical behavior differently. Therefore, fault zone investigations are important to determine which areas have potential for EGS applications and long-term sustainability.

6 Conclusion

The extensive experimental investigation of Schauinsland Mine fault zone revealed that mineralogical and petrographic characteristics, such as quartz content, hydrothermal alteration degree, and grain size, strongly influence the mechanical properties of the RFZ. These justify the differentiation of the fault zone into host rock, transition zone, and main core zone.

As expected, the gneiss of the host rock showed high strength values, high elastic properties, and low porosity and permeability values. These observations align with previous studies on intact and minimally-altered gneiss.

Samples next to the main core zone exhibited high compressive strength values, along with a tendency towards ductile behavior and high strain accumulation before and after reaching the maximum compressive strength. Unlike the host rock, these samples displayed plastic behavior and high porosity values. This can be attributed to the high content of hydrothermally-altered biotite and plagioclase, forming mixed clayey gouges. This leads to compaction and grain rearrangement to resist the applied stress. Therefore, despite their contrasting mineralogical and petrographic characteristics, both the host rock and the samples next to the main core zone achieve similar compressive strength through different mechanisms.

The transition zone is self-describing based on its name. It shows a transition between elastic and plastic behavior, characterized by less distinct brittle failure and higher strain rates. In terms of strength, the transition zone is weaker than the previously mentioned zones, which could potentially lead to reactivation at lower stresses, resulting in higher instability. Previous researches have shown that fault reactivation is supported by the amount of clay and altered material. While the clay content in our study is lower than in

previous research, the heterogeneity of the foliation and clayey gouges may contribute to reduce fault stability, especially in the transition zone and possibly close to the main core zone.

The interaction between the transtension of the ore vein and the mechanical properties of the surrounding rock led potentially to distinct deformation behaviors in different zones. Close to the main core zone, low tensile strength values resulted in smearing and ductile behavior, whereas the transition zone exhibited a mix of ductile and brittle behavior. In contrast, the host rock displayed high tensile strength values and underwent brittle deformation, ultimately leading to fracture development.

The data demonstrate that the mineralogical and petrographic characteristics strongly influence the mechanical properties of rocks, particularly in fault zones. Different areas exhibit significant variation in their behavior and stress resistance. This study can serve as an indicator for assessing the potential of different areas within a fault zone for EGS exploitation. Furthermore, the data highlights the importance of a detailed analysis of a wide range of rock characteristics, and integrating various research fields to understand the complex mechanisms governing fault zones.

Acknowledgements Many thanks to Tanja Ballerstedt, Florian Zimmermann and Christian Cunow from GFZ in Potsdam for their assistance in the sample preparation and execution of the experiments at the MTS, Mercury Porosimeter and Gas-Permeameter. Additionally, the authors would like to thank Ph.D. Julie Friddell for language editing. We thank the Schauinsland Mine staff for their warm welcome and support to study the mine galleries. Without each of them, this work would not have been possible to this extent.

Author Contribution Lena Muhl: Conceptualization, Methodology, Software, Formal analysis, Investigation, Resources, Data Curation, Writing – Original Draft, Writing – Review & Editing, Visualization. Benjamin Avakian: Conceptualization, Methodology, Software, Formal analysis, Investigation, Resources, Data Curation, Writing – Original Draft, Writing – Review & Editing, Visualization. Guido Blöcher: Validation, Writing- Review & Editing, Visualization, Supervision. Ingo Sass: Writing – Review & Editing, Funding, Supervision. Ghislain Trullenque: Writing – Review & Editing, Funding, Supervision.

Funding Open Access funding enabled and organized by Projekt DEAL. This study was supported by European Union's Horizon 2020 Research and Innovation program under grant agreement no.792037 (H2020 MEET project). It was also supported by the EUTOPIA European University network which provided a PhD grant. Moreover, the research was supported by the GeoLaB project fund by the Helmholtz association.

Data availability The data supporting the findings of this study are available from the corresponding authors upon request.

Declarations

Competing interests This study was supported by European Union's Horizon 2020 Research and Innovation program under grant agreement no.792037 (H2020 MEET project). It was also supported by the EUTOPIA European University network which provided a PhD grant.

References

Acosta M, Violay M (2020) Mechanical and hydraulic transport properties of transverse-isotropic gneiss deformed under deep reservoir stress and pressure conditions. Int J Rock Mech Min Sci 130:104235. https://doi.org/10.1016/j.ijrmms.2020.104235

Agliardi F, Zanchetta S, Crosta GB (2014) Fabric controls on the brittle failure of folded gneiss and schist. Tectonophysics 637:150–162. https://doi.org/10.1016/j.tecto.2014.10.006

Altherr R, Henes-Klaiber U, Hegner E, Satir M, Langer C (1999) Plutonism in the Variscan Odenwald (Germany): from subduction to collision. Int J Earth Sci 88:422–443. https://doi.org/10.1007/s005310050276

Altherr R, Holl A, Hegner E, Langer C, Kreuzer H (2000) High-potassium, calc-alkaline I-type plutonism in the European Variscides: northern Vosges (France) and northern Schwarzwald (Germany). Lithos 50:51–73. https://doi.org/10.1016/S0024-4937(99)00052-3

Altherr R, Hepp S, Klein H, Hanel M (2021) Metabasic rocks from the Variscan Schwarzwald (SW Germany): metamorphic evolution and igneous protoliths. Int J Earth Sci (Geol Rundsch) 110:1293–1319. https://doi.org/10.1007/s00531-021-02016-w

ASTM International (2014). ASTM D7012-14: Standard Test methods for Compressive Strength and Elastic Moduli of Intact Rock Core Specimens under Varying States of Stress and Temperatures. https://doi.org/10.1520/D7012-14

Avakian B, Ledésert BA, Trullenque G, Hébert RL, Klee J, Potel S, Miloikovitch T, Goderis S, Claeys P (2025) Structural inheritance and hydrothermal alteration impact on fluid circulation in a clay-rich shear zone. J Struct Geol 190:105296. https://doi.org/10.1016/j.jsg.2024.105296

Bai Q, Young RP (2020) Numerical investigation of the mechanical and damage behaviors of veined gneiss during true-triaxial stress path loading by simulation of in situ conditions. Rock Mech Rock Eng 53:133–151. https://doi.org/10.1007/s00603-019-01898-2

Bauer JF, Krumbholz M, Meier S, Tanner DC (2017) Predictability of properties of a fractured geothermal reservoir: the opportunities and limitations of an outcrop analogue study. Geotherm Energy 5:24. https://doi.org/10.1186/s40517-017-0081-0

Baujard C, Genter A, Dalmais E, Maurer V, Hehn R, Rosillette R, Vidal J, Schmittbuhl J (2017) Hydrothermal characterization of wells GRT-1 and GRT-2 in Rittershoffen, France: implications on the understanding of natural flow systems in the rhine graben. Geothermics 65:255–268. https://doi.org/10.1016/j.geothermics.2016.11.001

Bedford JD, Faulkner DR, Lapusta N (2022) Fault rock heterogeneity can produce fault weakness and reduce fault stability. Nat Commun 13:326. https://doi.org/10.1038/s41467-022-27998-2

Bergerat F (1985) Déformations cassantes et champs de contrainte tertiaires dans la plate-forme européenne. Dissertation, Université Pierre et Marie Curie-Paris VI.

Bertrand L, Géraud Y, Diraison M (2021) Petrophysical properties in faulted basement rocks: insights from outcropping analogues on the West European Rift shoulders. Geothermics 95:102144. https://doi.org/10.1016/j.geothermics.2021.102144

Bischoff A, Heap MJ, Mikkola P, Kuva J, Reuschlé T, Jolis EM, Engström J, Reijonen H, Leskelä T (2024) Hydrothermally altered shear zones: a new reservoir play for the expansion of deep geothermal exploration in crystalline settings. Geothermics 118:102895. https://doi.org/10.1016/j.geothermics.2023.102895

Boese CM, Kwiatek G, Fischer T, Plenkers K, Starke J, Blümle F, Janssen C, Dresen G (2022) Seismic monitoring of the STIMTEC hydraulic stimulation experiment in anisotropic metamorphic gneiss. Solid Earth 13(2):323–346. https://doi.org/10.5194/se-13-323-2022

Bossennec C, Seib L, Frey M, Van Der Vaart J, Sass I (2022) Structural architecture and permeability patterns of crystalline reservoir rocks in the Northern Upper Rhine Graben: insights from surface analogues of the Odenwald. Energies 15:1310. https://doi.org/10.3390/en15041310

Brace WF, Walsh JB, Frangos WT (1968) Permeability of granite under high pressure. J Geophys Res 73(6):2225–2236. https://doi.org/10.1029/JB073i006p02225

Bremer J, Kohl T, Sass I, Kolditz O, Rudolph B, Rühaak W et al (2025) GeoLaB annual report 2024. GeoLab. https://doi.org/10.5445/IR/1000184950

Caine JS, Evans JP, Forster CB (1996) Fault zone architecture and permeability structure. Geol 24:1025. https://doi.org/10.1130/0091-7613(1996)024%3c1025:FZAAPS%3e2.3.CO;2

Callahan OA, Eichhubl P, Davatzes NC (2020) Mineral precipitation as a mechanism of fault core growth. J Struct Geol 140:104156. https://doi.org/10.1016/j.jsg.2020.104156

Chabani A, Trullenque G, Ledésert BA, Klee J (2021) Multiscale characterization of fracture patterns: a case study of the Noble Hills Range (Death Valley, CA, USA), application to geothermal reservoirs. Geosciences 11:280. https://doi.org/10.3390/geosciences11070280

Choi J-H, Edwards P, Ko K, Kim Y-S (2016) Definition and classification of fault damage zones: a review and a new methodological approach. Earth-Sci Rev 152:70–87. https://doi.org/10.1016/j.earscirev.2015.11.006

Cuenot N, Charléty J, Dorbath L, Haessler H (2006) Faulting mechanisms and stress regime at the European HDR site of Soultz-sous-Forêts, France. Geothermics 35:561–575. https://doi.org/10.1016/j.geothermics.2006.11.007

Dezayes C, Lerouge C, Innocent C, Lach P (2021) Structural control on fluid circulation in a graben system: constraints from the Saint Pierre Bois quarry (Vosges, France). J Struct Geol 146:104323. https://doi.org/10.1016/j.jsg.2021.104323

Doubre C, Meghraoui M, Masson F, Lambotte S, Jund H, Bès De Berc M, Grunberg M (2022) Seismotectonics in Northeastern France and neighboring regions. Comptes Rendus Géoscience 353:153–185. https://doi.org/10.5802/crgeos.80

Duwiquet H, Guillou-Frottier L, Arbaret L, Bellanger M, Guillon T, Heap MJ (2021) Crustal fault zones (CFZ) as geothermal power systems: a preliminary 3D THM model constrained by a multidisciplinary approach. Geofluids 2021:1–24. https://doi.org/10.1155/2021/8855632

Edel J-B, Schulmann K (2009) Geophysical constraints and model of the "Saxothuringian and Rhenohercynian subductions – magmatic arc system" in NE France and SW Germany. Bulletin De La Société Géologique De France 180:545–558. https://doi.org/10.2113/gssgfbull.180.6.545

Edel J-B, Whitechurch H, Diraison M (2006) Seismicity wedge beneath the Upper Rhine Graben due to backwards Alpine push? Tectonophysics 428:49–64. https://doi.org/10.1016/j.tecto.2006.08.009

Fairhurst C (1964) On the Validity of the 'Brazilian' test for brittle materials. Int. J. Rock Mech Mining Sci. 1(4):535–546

Faulkner DR, Rutter EH (2001) Can the maintenance of overpressured fluids in large strike-slip fault zones explain their apparent weakness? Geol 29:503. https://doi.org/10.1130/0091-7613(2001)029%3c0503:CTMOOF%3e2.0.CO;2

Faulkner DR, Jackson CAL, Lunn RJ, Schlische RW, Shipton ZK, Wibberley CAJ, Withjack MO (2010) A review of recent developments concerning the structure, mechanics and fluid flow properties of fault zones. J Struct Geol 32:1557–1575. https://doi.org/10.1016/j.jsg.2010.06.009

Faulkner DR, Mitchell TM, Rutter EH, Cembrano J (2008) On the structure and mechanical properties of large strike-slip faults. SP 299:139–150. https://doi.org/10.1144/SP299.9

Fossen H, Cavalcante GCG (2017) Shear zones—a review. Earth-Sci Rev 171:434–455. https://doi.org/10.1016/j.earscirev.2017.05.002

Garcia J, Hartline C, Walters M, Wright M, Rutqvist J, Dobson PF, Jeanne P (2016) The Northwest Geysers EGS Demonstration Project, California. Geothermics 63:97–119. https://doi.org/10.1016/j.geothermics.2015.08.003

Genter A, Traineau H, Dezayes Ch, Elsass P, Ledesert B, Meunier A, Villemin T (1996) Fracture analysis and reservoir characterization of the granitic basement in the HDR Soultz Project (France). Int J Rock Mech Min Sci Geomech Abstracts 33:189–214. https://doi.org/10.1016/0148-9062(96)83915-5

Genter A, Evans K, Cuenot N, Fritsch D, Sanjuan B (2010) Contribution of the exploration of deep crystalline fractured reservoir of Soultz to the knowledge of enhanced geothermal systems (EGS). C R Geoscience 342:502–516. https://doi.org/10.1016/j.crte.2010.01.006

Geyer OF, Gwinner MP, Geyer M, Nitsch E, Simon T, Ellwanger D (2011) Geologie von Baden-Württemberg, 5, völlig neu bearb, Aufl. Schweizerbart, Stuttgart

Glaas C, Vidal J, Genter A (2021) Structural characterization of naturally fractured geothermal reservoirs in the central Upper Rhine Graben. J Struct Geol 148:104370. https://doi.org/10.1016/j.jsg.2021.104370

Griffith AA (1924) The theory of rupture, in: International Congress for Applied Mechanics.

Guo H, Aziz NI, Schmidt LC (1993) Rock fracture-toughness determination by the Brazilian test. Eng Geol 33:177–188. https://doi.org/10.1016/0013-7952(93)90056-I

Häge M, Joswig M (2009) Spatiotemporal distribution of aftershocks of the 2004 December 5 M L = 5.4 Waldkirch (Germany) earthquake. Geophys J Int 178:1523–1532. https://doi.org/10.1111/j.1365-246X.2009.04235.x

He C, Mishra B, Shi Q, Zhao Y, Lin D, Wang X (2023) Correlations between mineral composition and mechanical properties of granite using digital image processing and discrete element method. Int J Min Sci Technol 33:949–962. https://doi.org/10.1016/j.ijmst.2023.06.003

Heidbach O, Rajabi M, Reiter K, Ziegler M (2016). World Stress Map (2016) https://doi.org/10.5880/WSM.2016.002

Herron M, Loan M, Charsky A, Herron SL, Pomerantz AE, Polyakov M (2014). Clay Typing, Mineralogy, Kerogen Content and Kerogen Characterization from DRIFTS Analysis of Cuttings or Core. In: Proceedings of the 2nd unconventional resources technology conference. Presented at the unconventional resources technology conference, American association of petroleum Geologists, Denver, Colorado, USA. https://doi.org/10.15530/urtec-2014-1922653

Hofmann H, Blöcher G, Börsing N, Maronde N, Pastrik N, Zimmermann G (2014) Potential for enhanced geothermal systems in low permeability limestones—stimulation strategies for the Western Malm karst (Bavaria). Geothermics 51:351–367. https://doi.org/10.1016/j.geothermics.2014.03.003

Hofmann H, Babadagli T, Yoon JS, Zang A, Zimmermann G (2015) A grain based modeling study of mineralogical factors affecting strength, elastic behavior and micro fracture development during compression tests in granites. Eng Fract Mech 147:261–275. https://doi.org/10.1016/j.engfracmech.2015.09.008

Illies JH, Rothé JP, Sauer K (1967) Development and tectonic pattern of the Rhinegraben. The Rhinegraben Progress Report. Abh Geol Landesamt Baden-Würtemberg 6:7–9

Illies JH, Greiner G (1979) Holocene movements and state of stress in the Rhinegraben rift system. In: Developments in Geotectonics. Elsevier, pp 349–359. https://doi.org/10.1016/B978-0-444-41783-1.50057-X

Jaeger JC, Cook NGW, Zimmerman RW (2007) Fundamentals of rock mechanics, 4th edn. Blackwell, Malden

Jones C, Simmons S, Moore J (2024) Geology of the Utah Frontier Observatory for Research in Geothermal Energy (FORGE) Enhanced Geothermal System (EGS) site. Geothermics 122:103054. https://doi.org/10.1016/j.geothermics.2024.103054

Klee J, Potel S, Ledésert BA, Hébert RL, Chabani A, Barrier P, Trullenque G (2021a) Fluid-rock interactions in a paleo-geothermal reservoir (Noble Hills Granite, California, USA). Part 1: Granite pervasive alteration processes away from fracture zones. Geosciences 11:325. https://doi.org/10.3390/geosciences11080325

Klee J, Chabani A, Ledésert BA, Potel S, Hébert RL, Trullenque G (2021b) Fluid-rock interactions in a paleo-geothermal reservoir (Noble Hills Granite, California, USA). Part 2: The influence of fracturing on granite alteration processes and fluid circulation at low to moderate regional strain. Geosciences 11:433. https://doi.org/10.3390/geosciences11110433

Kluge C, Blöcher G, Barnhoorn A, Schmittbuhl J, Bruhn D (2021) Permeability evolution during shear zone initiation in low-porosity rocks. Rock Mech Rock Eng 54:5221–5244. https://doi.org/10.1007/s00603-020-02356-0

Krohe A, Eisbacher GH (1988) Oblique crustal detachment in the Variscan Schwarzwald, southwestern Germany. Geol Rundsch 77:25–43. https://doi.org/10.1007/BF01848674

Lagarde J-L, Capdevila R, Fourcade S (1992) Granites et collision continentale: l'exemple des granitoïdes carbonifères dans la chaîne hercynienne ouest-européenne. Bulletin-Societe Geologique De France 163:597–597

Lan H, Martin CD, Hu B (2010) Effect of heterogeneity of brittle rock on micromechanical extensile behavior during compression loading. J Geophys Res 115:B01202. https://doi.org/10.1029/2009JB006496

Larroque JM, Etchecopar A, Philip H (1987) Evidence for the permutation of stresses σ1 and σ2 in the Alpine foreland: the example of the Rhine graben. Tectonophysics 144:315–322. https://doi.org/10.1016/0040-1951(87)90299-X

Ledésert B, Berger G, Meunier A, Genter A, Bouchet A (1999) Diagenetic-type reactions related to hydrothermal alteration in the Soultz-sous-Forêts granite, France. Ejm 11:731–742. https://doi.org/10.1127/ejm/11/4/0731

Ledingham P, Cotton L, Law R (2019) The United Downs Deep Geothermal Power Project. Proceedings Workshop on Geothermal Reservoir Engineering, Stanford University, California, USA

Lee TJ, Song Y, Yoon WS, Kim K-Y, Jeon J, Min K-B, Cho Y-H (2011) The first enhanced geothermal system project in Korea

Li D, Wong LNY (2013) The Brazilian disc test for rock mechanics applications: review and new insights. Rock Mech Rock Eng 46:269–287. https://doi.org/10.1007/s00603-012-0257-7

Logan JM, Rauenzahn KA (1987) Frictional dependence of gouge mixtures of quartz and montmorillonite on velocity, composition and fabric. Tectonophysics 144:87–108. https://doi.org/10.1016/0040-1951(87)90010-2

Lu Z, He C (2018) Friction of foliated fault gouge with a biotite interlayer at hydrothermal conditions. Tectonophysics 740:72–92. https://doi.org/10.1016/j.tecto.2018.05.003

Marone C (1995) Fault zone strength and failure criteria. Geophys Res Lett 22:723–726

Meixner J, Schill E, Gaucher E, Kohl T (2014) Inferring the in situ stress regime in deep sediments: an example from the Bruchsal geothermal site. Geotherm Energy 2:7. https://doi.org/10.1186/s40517-014-0007-z

Meller C, Ledésert B (2017) Is there a link between mineralogy, petrophysics, and the hydraulic and seismic behaviors of the Soultz-sous-Forêts granite during stimulation? A review and reinterpretation of petro-hydromechanical data toward a better understanding of induced seismicity: petro-hydromechanics of Soultz granite. J Geophys Res Solid Earth 122:9755–9774. https://doi.org/10.1002/2017JB014648

Morrow CA, Shi LQ, Byerlee JD (1984) Permeability of fault gouge under confining pressure and shear stress. J Geophys Res 89:3193–3200. https://doi.org/10.1029/JB089iB05p03193

Peacock DCP, Sanderson DJ, Leiss B (2021) Use of Mohr diagrams to predict fracturing in a potential geothermal reservoir. Geosciences 11:501. https://doi.org/10.3390/geosciences11120501

Peacock DCP, Sanderson DJ, Leiss B (2022) Use of analogue exposures of fractured rock for enhanced geothermal systems. Geosciences 12:318. https://doi.org/10.3390/geosciences12090318

Pei L, Blöcher G, Milsch H, Zimmermann G, Sass I, Huenges E (2018) Thermo-mechanical properties of upper Jurassic (Malm) carbonate rock under drained conditions. Rock Mech Rock Eng 51:23–45. https://doi.org/10.1007/s00603-017-1313-0

Peng S, Zhang J (2007) Engineering geology for underground rocks. Springer, Berlin

Pfaff K, Romer RL, Markl G (2009) U-Pb ages of ferberite, chalcedony, agate, "U-mica" and pitchblende: constraints on the mineralization history of the Schwarzwald ore district. Eur J Mineral 21:817–836. https://doi.org/10.1127/0935-1221/2009/0021-1944

Rotstein Y, Schaming M (2011) The upper Rhine Graben (URG) revisited: miocene transtension and transpression account for the observed first-order structures. Tectonics 30:2010TC002767. https://doi.org/10.1029/2010TC002767

Saadat M, Taheri A (2019) A numerical approach to investigate the effects of rock texture on the damage and crack propagation of a pre-cracked granite. Comput Geotech 111:89–111. https://doi.org/10.1016/j.compgeo.2019.03.009

Sajid M, Coggan J, Arif M, Andersen J, Rollinson G (2016) Petrographic features as an effective indicator for the variation in strength of granites. Eng Geol 202:44–54. https://doi.org/10.1016/j.enggeo.2016.01.001

Schmittbuhl J, Lambotte S, Lengliné O, Grunberg M, Jund H, Vergne J, Cornet F, Doubre C, Masson F (2022) Induced and triggered seismicity below the city of Strasbourg, France from November 2019 to January 2021. Comptes Rendus Géosci 353:561–584. https://doi.org/10.5802/crgeos.71

Schulz KE, Bär K, Sass I (2022) Lab-scale permeability enhancement by chemical treatment in fractured granite (Cornubian Batholith) for the United Downs Deep Geothermal Power Project, Cornwall (UK). Geosciences (Basel) 12:35. https://doi.org/10.3390/geosciences12010035

Schumacher ME (2002) Upper Rhine Graben: Role of preexisting structures during rift evolution: UPPER RHINE GRABEN EVOLUTION. Tectonics 21, 6-1-6–17. https://doi.org/10.1029/2001TC900022

Sibson RH (1992) Implications of fault-valve behaviour for rupture nucleation and recurrence. Tectonophysics 211:283–293. https://doi.org/10.1016/0040-1951(92)90065-E

Sittler C (1985) Les hydrocarbures d'Alsace dans le contexte historique et géodynamique du fossé rhénan. Bull Cent Rech Elf Explor Prod 2:335–371

Tenthorey E, Cox SF (2006) Cohesive strengthening of fault zones during the interseismic period: an experimental study. J Geophys Res 111:2005JB004122. https://doi.org/10.1029/2005JB004122

Terzaghi K (1925) Erdbaumechanik auf Bodenphysikalischer Grundlage. Franz Deuticke, Liepzig-Vienna

Thermo Scientific (2019) PASCAl Evo Series Mercury Porisimeters and SOL.I.D Evo Software Operating Manual. ThermoFisher.

Tuğrul A, Zarif IH (1999) Correlation of mineralogical and textural characteristics with engineering properties of selected granitic rocks from Turkey. Eng Geol 51:303–317. https://doi.org/10.1016/S0013-7952(98)00071-4

Villemin T, Bergerat F (1987) L'evolution structurale du fosse rhenan au cours du Cenozoique ; un bilan de la deformation et des effets thermiques de l'extension. Bull Soc Geol Fr. https://doi.org/10.2113/gssgfbull.III.2.245

Wang C, Lin W, Wu FT (1978) Constitution of the San Andreas Fault Zone at depth. Geophys Res Lett 5:741–744. https://doi.org/10.1029/GL005i009p00741

Werner W, Franzke HJ, Wirsing G, Jochum J, Steiber B (2002) Bergbau, Geologie, Hydrogeologie, Mineralogie, Geochemie, Tektonik und Lagerstättenentstehung 114

Whitney DL, Evans BW (2010) Abbreviations for names of rock-forming minerals. Am Mineral 95:185–187. https://doi.org/10.2138/am.2010.3371

Wittenbrink J (1999) Diplomkartierung (Teil A) Petrographische und tektonische Kartierung des Zentralschwarzwälder Gneiskomplexes im Bereich der Blei – Zink – Lagerstätte Schauinsland bei Freiburg i. Br./Schwarzwald (Master Thesis). Technische Universität Clausthal

Wong LNY, Peng J, Teh CI (2018) Numerical investigation of mineralogical composition effect on strength and micro-cracking behavior of crystalline rocks. J Nat Gas

Sci Eng 53:191–203. https://doi.org/10.1016/j.jngse.2018.03.004

Ziegler PA (1992) European Cenozoic rift system. Tectonophysics 208:91–111. https://doi.org/10.1016/0040-1951(92)90338-7

Ziegler PA, Dèzes P (2005) Evolution of the lithosphere in the area of the Rhine Rift System. Int J Earth Sci 94:594–614. https://doi.org/10.1007/s00531-005-0474-3

Ziegler PA, Schumacher ME, Dèzes P, Van Wees J-D, Cloetingh S (2006) Post-Variscan evolution of the lithosphere in the area of the European Cenozoic Rift System. Mem 32:97–112. https://doi.org/10.1144/GSL.MEM.2006.032.01.06